Research Square

Preprints are preliminary reports that have not undergone peer review.
They should not be considered conclusive, used to inform clinical practice,
or referenced by the media as validated information.

Carrier-Free Supramolecular Co-Assembly Enables Oxygen-Economizing Photodynamic Therapy via Mitochondrial Respiration Suppression

Xin Xie
Guangdong Medical University
Tao Quan
Guangdong Medical University
Haiqian Zhang
Guangdong Medical University
Rui Liang
Guangdong Medical University
Yong Huang
Guangdong Medical University
Lihe Sun
Guangdong Medical University
Fengmin Xiu
Guangdong Medical University
Biao Zheng
Guangdong Medical University
Shangjun Zhou
Dongguan Hospital of Guangzhou University of Chinese Medicine
Chaohui Zhen
Guangdong Medical University
Xinsheng Peng
Guangdong Medical University
Bowen Li
bowen_li@ahmu.edu.cn

Anhui Medical University

Research Article

Keywords: Photodynamic therapy, Hypoxia, Carrier-free, Oxygen-economizing strategy, Self-assembly, Mitochondrial respiration inhibition

Posted Date: September 11th, 2026

DOI: https://doi.org/10.21203/rs.3.rs-10867673/v1

License: This work is licensed under a Creative Commons Attribution 4.0 International License.
Read Full License

Additional Declarations: No competing interests reported.

Abstract

Hypoxia within the tumor microenvironment severely compromises the therapeutic efficacy of photodynamic therapy (PDT) by limiting oxygen-dependent reactive oxygen species (ROS) generation. Although extensive efforts have been devoted to oxygen-supplementation strategies, most existing approaches provide only transient hypoxia relief and are hindered by limited oxygen-loading capacity, premature oxygen leakage, and insufficient catalytic efficiency. Herein, we report a carrier-free self-assembly nanodrug (BBR-Ce6 NPs) that enhances PDT through a durable oxygen-economizing strategy by reducing mitochondrial oxygen consumption rather than directly supplying oxygen. The nanodrug is composed of the mitochondria-targeting oxidative phosphorylation (OXPHOS) inhibitor berberine (BBR) and the clinically used photosensitizer chlorin e6 (Ce6), which spontaneously co-assemble via synergistic π-π stacking and hydrogen-bonding interactions to form stable nanoparticles with high drug-loading efficiency. Benefiting from reversible noncovalent interactions, BBR-Ce6 NPs gradually disassemble within the mildly acidic tumor microenvironment, enabling tumor-responsive drug release. Following cellular internalization, BBR preferentially accumulates in mitochondria and inhibits mitochondrial complex I activity, thereby suppressing OXPHOS, reducing cellular oxygen consumption, and durably alleviating tumor hypoxia. This oxygen-sparing effect markedly enhances Ce6-mediated ROS generation and significantly improves PDT efficacy both in vitro and in vivo. In addition, the carrier-free formulation minimizes excipient-associated toxicity while simplifying nanoparticle fabrication. Collectively, this study establishes a safe and sustained hypoxia-relief strategy for enhancing PDT efficacy and offers a versatile nanoplatform for combining natural mitochondrial modulators with photosensitizers to overcome hypoxia-associated resistance of PDT in cancer treatment.

1. Introduction

Photodynamic therapy (PDT) has emerged as a highly attractive modality for cancer treatment because of its non-invasive nature, precise spatiotemporal controllability, minimal systemic toxicity, and low propensity to induce drug resistance. Upon light irradiation, photosensitizers transfer absorbed energy to molecular oxygen to generate cytotoxic reactive oxygen species (ROS), particularly singlet oxygen ($^1O_2$), which induce tumor cell apoptosis and necrosis [1–4]. Despite these unique advantages, the therapeutic efficacy of PDT is intrinsically dependent on oxygen availability, creating a fundamental contradiction in solid tumors, where hypoxia is a typical characteristic of the tumor microenvironment (TME) [5–7]. Owing to aberrant vascular architecture, rapid proliferation, and elevated metabolic demand, tumor tissues frequently experience insufficient oxygen supply, which severely limits ROS generation during PDT [8]. Moreover, the photodynamic process itself consumes substantial amounts of oxygen, further aggravating local hypoxia and establishing a vicious cycle that progressively undermines therapeutic efficacy [9]. Consequently, overcoming tumor hypoxia has become one of the serve challenges and most critical prerequisites for maximizing the therapeutic potential of PDT.

To address this challenge, numerous oxygen-supplement strategies have been developed, including oxygen carriers such as perfluorocarbons and hemoglobin-based systems [10–12], as well as catalytic

platforms that decompose endogenous hydrogen peroxide (H_2O_2) to generate oxygen in situ [13, 14]. Although these approaches have demonstrated promising results, their therapeutic benefits are often transient [15]. Oxygen carriers typically suffer from limited loading capacity and premature leakage, while catalytic systems are restricted by insufficient endogenous H_2O_2 levels and relatively low conversion efficiency [16]. More importantly, most of these approaches provide only transient relief of hypoxia and fail to achieve sustained and effective reprogramming of TME [17]. Therefore, the development of safe and long-lasting strategies to alleviate tumor hypoxia remains highly desirable for maximizing PDT efficacy. Recently, an alternative and potentially more durable strategy is to reduce cellular oxygen consumption rather than directly supply oxygen [18–21]. As mitochondria are the principal sites of oxygen consumption via oxidative phosphorylation (OXPHOS), inhibition of mitochondrial respiration can effectively conserve intracellular oxygen and thereby enhance local oxygen availability for ROS generation during PDT [22]. Guided by this concept, several OXPHOS inhibitors, including atovaquone [23, 24], metformin [25], and papaverine [26], have been investigated to enhance photodynamic therapy outcomes. However, since OXPHOS occurs exclusively within mitochondria, the success of this strategy critically depends on the efficient delivery of inhibitors to this key organelle [27, 28]. Unfortunately, most conventional OXPHOS inhibitors lack intrinsic mitochondrial-targeting capability and often exhibit insufficient mitochondrial accumulation, thereby substantially limiting their ability to suppress respiration and relieve tumor hypoxia.

Berberine (BBR), a natural isoquinoline alkaloid isolated from *Coptis chinensis*, has attracted increasing interest owing to its good biosafety, low cost, and diverse pharmacological activities, including anticancer effects [29, 30]. Importantly, BBR possesses an intrinsic mitochondria-targeting capability attributable to its delocalized lipophilic cationic structure, which enables selective accumulation within mitochondria [31]. Once localized to this critical organelle, BBR inhibits mitochondrial complex I, thereby suppressing OXPHOS, reducing cellular oxygen consumption, and increasing oxygen availability for PDT [32–34]. These unique properties make BBR an ideal oxygen-economizing agent for overcoming tumor hypoxia and enhancing PDT efficacy. In addition, compared with conventional synthetic respiratory inhibitors, BBR offers the advantages of well-established biosafety, low systemic toxicity, and strong translational potential. However, despite its considerable therapeutic promise, the pharmaceutical application of BBR remains substantially limited by its poor aqueous solubility, unfavorable pharmacokinetic behavior, and low bioavailability, all of which hinder its efficient systemic delivery and accumulation at tumor sites [35].

Recent advances in nanomedicine have demonstrated that drug molecules with large π-conjugated frameworks and abundant noncovalent interaction sites are particularly well suited for self-assembly through π-π stacking, hydrogen bonding, and hydrophobic interactions [36, 37]. Such self-assembly offers an effective strategy for the co-delivery of poorly soluble therapeutics by integrating multiple drug molecules into a single nanostructure without the use of pharmacologically inert carriers [38, 39]. Compared with conventional nanocarriers, carrier-free nanodrugs possess several notable advantages, including high drug loading, simplified formulation, and minimized carrier-associated toxicity [40–42]. In

addition, because these nanostructures are stabilized by reversible noncovalent interactions, they can undergo gradual disassembly under the mildly acidic conditions of TME, enabling controlled drug release and improving the precision of tumor-specific therapy [43, 44]. Interestingly, BBR possesses a rigid planar π-conjugated structure that readily participates in intermolecular π-π stacking and other non-covalent interactions, making it particularly suitable for self-assembly [45, 46]. Notably, the clinically used photosensitizer chlorin e6 (Ce6) also contains an extended aromatic framework and amphiphilic features that enable spontaneous self-assembly [47, 48]. We therefore hypothesized that BBR and Ce6 could directly co-assemble into stable carrier-free nanoparticles through synergistic π-π stacking, electrostatic interactions, and hydrophobic effects, enabling synchronized delivery of both therapeutic components with exceptionally high drug loading and tumor-responsive release.

Herein, we developed a carrier-free self-assembled nanodrug (BBR-Ce6 NPs) composed solely of the mitochondria-targeting OXPHOS inhibitor BBR and the photosensitizer Ce6 to enhance PDT through efficient and sustained alleviation of tumor hypoxia (Scheme 1). BBR and Ce6 spontaneously co-assemble into structurally stable nanoparticles with high drug-loading efficiency and good colloidal stability. Following systemic administration, BBR-Ce6 NPs accumulate efficiently in tumor tissue and are readily internalized by cancer cells. Under the mildly acidic tumor microenvironment, the nanoparticles gradually disassemble and release both therapeutic components. The released BBR selectively targets mitochondria and inhibits complex I activity, thereby disrupting the electron transport chain and markedly reducing cellular respiratory oxygen consumption. This oxygen-sparing effect durably alleviates tumor hypoxia and significantly enhances Ce6-mediated ROS generation under light irradiation, resulting in substantially improved photodynamic antitumor efficacy. This work establishes a safe and long-acting oxygen-economizing strategy and provides a versatile supramolecular platform for integrating natural mitochondrial modulators with photosensitizers to overcome hypoxia-associated resistance in cancer photodynamic therapy.

2. Results and discussion

2.1. Preparation and characterization of BBR-Ce6 NPs

The planar structure of Ce6 endows it with hydrophobicity and enables π-π stacking, while its three carboxylic acid groups provide sites for hydrogen bonding and electrostatic interactions. Together, these features allow Ce6 to participate in noncovalent, intermolecular self-assembly with diverse drug compounds [49–51]. Likewise, BBR contains three aromatic rings with sufficient planarity, allowing it to co-assemble with Ce6 through π-π stacking interactions. Carrier-free fabrication of BBR-Ce6 NPs was to be achieved through the direct self-assembly of BBR and Ce6. To optimize nanoparticle size distribution for enhanced tumor accumulation via enhanced permeability and retention (EPR) effect, BBR-Ce6 NPs were prepared at various molar feeding ratios, and their hydrodynamic diameters were characterized by dynamic light scattering (DLS). As shown in Fig. 1A, 1B and Table S1, nanoparticles fabricated at a 1:1 ratio exhibited the smallest hydrodynamic diameter (116.2 nm) and the narrowest polydispersity (PDI = 0.153). Transmission electron microscopy (TEM) imaging further confirmed their uniform spherical

morphology (Fig. 1C). Moreover, these nanoparticles maintained stable average sizes and PDIs over one week of storage, indicating good colloidal stability in aqueous solution (Fig. S1). When dispersed in DMED supplemented with 10% FBS, BBR-Ce6 NPs showed slightly increased diameters and PDIs compared to those in water, a change attributed to the formation of a protein corona on the nanoparticle surface (Fig. S2). Based on these results, the 1:1 formulation was selected for subsequent studies. Drug loading efficiencies were quantified by UV-vis spectroscopy and HPLC calibration curves (Fig. S3 and S4), yielding values of 52.8% for Ce6 and 47.2% for BBR. Additionally, BBR-Ce6 NPs displayed slightly negative zeta potential (− 14.0 mV, Fig. S5), a property that may minimize serum protein adsorption and thereby prolong blood circulation time.

UV-vis absorption spectra of BBR-Ce6 NPs displayed characteristic peaks corresponding to BBR (265 and 348 nm) and Ce6 (406 nm), confirming successful nanoparticle formation (Fig. 1D). Following assembly, the characteristic Ce6 peak at 664 nm red-shifted to 700 nm, accompanied by a slight decrease in absorbance. Fluorescence emission spectra further revealed a significant reduction in the fluorescence intensity of the nanoparticles relative to free Ce6 (Fig. 1E). These spectral changes indicated intermolecular interactions between the two components. To elucidate the driving forces underlying this self-assembly, we monitored the UV-vis spectral changes of BBR-Ce6 NPs under varying dispersion conditions. As shown in Fig. 1F, the absorption profile remained stable in the presence of 2 mM NaCl or 0.2% sodium dodecyl sulfate (SDS). By contrast, dissolution in DMSO restored the original Ce6 absorption peak, indicating disruption of the π-π stacking interactions within the nanoparticles. Additionally, the absorption spectrum of BBR-Ce6 NPs exhibited slight changes with increasing urea concentrations, suggesting the contribution of weak hydrogen bonding (Fig. 1G). Collectively, these results indicated that π-π interactions serve as the primary driving force for the self-assembly of BBR-Ce6 NPs, with hydrogen bonding playing a secondary role.

Fourier transform infrared (FTIR) spectroscopy was performed on BBR, Ce6, and BBR-Ce6 NPs. The characteristic carbonyl stretching vibration of Ce6 at 1711 cm^{-1} shifted to 1568 cm^{-1} in the nanoparticles (Fig. S6), providing further evidence for hydrogen bonding and π-π stacking between the two components. The ROS generation capability of Ce6 before and after nano-formulation was subsequently evaluated using the singlet oxygen sensor green (SOSG) probe. BBR-Ce6 NPs generated $^1O_2$ at levels comparable to those of free Ce6 (Fig. S7), indicating that the self-assembly process did not compromise the photodynamic activity of Ce6. Finally, drug release profiles were examined at different pH values. At pH 5.0, both BBR and Ce6 exhibited markedly accelerated release kinetics and elevated cumulative release compared to pH 7.4 (Fig. 1H and I). This pH-dependent release behavior likely arises from the disruption of hydrogen bonds within the nanoparticles under acidic conditions, which gradually compromises their colloidal stability [52].

2.2. Self-assembly mechanism of BBR-Ce6 NPs

Molecular dynamics (MD) simulations were performed to elucidate the structural features of the final self-assembled BBR-Ce6 NPs and to identify the primary intermolecular driving forces underlying the

assembly process. BBR and Ce6 molecules were randomly distributed in a cubic simulation box, which was subsequently solvated with water molecules. Over the 100-ns simulation period, molecular aggregation was monitored through periodic snapshot analysis. Within the first 20 ns, BBR and Ce6 molecules formed small aggregates that underwent gradual structural reorganization, ultimately yielding compact, nearly spherical clusters by 100 ns (Fig. 2A and 2B). Notably, the system evolved into a sandwich-like architecture comprising BBR/Ce6/BBR layers (Fig. 2C). The principal driving force for self-assembly was identified as π-π stacking between the extended conjugated system of Ce6 and the three benzene rings of BBR, with additional stabilization provided by hydrogen bonds between the terminal hydroxyl group of Ce6 and oxygen atoms on BBR. To further characterize the conformational dynamics, the solvent-accessible surface area (SASA), radius of gyration (Rg), and root-mean-square deviation (RMSD) were computed throughout the simulation. Given that the solvent-exposed surface area progressively decreases during self-assembly, SASA serves as an effective metric for assessing nanoparticle compactness. A sharp decrease in SASA from 263.5 nm^2 to 200.7 nm^2 was observed within the first 1.5 ns, followed by a gradual decline to 111.4 nm^2 by 100 ns (Fig. 2D). This trajectory reflects rapid initial association of the two species into small clusters, followed by progressive compaction to minimize solvent exposure. Concomitantly, the number of hydrogen bonds between the complex and surrounding water molecules decreased steadily, indicating reduced aqueous interactions upon aggregation and thereby corroborating the self-assembly process (Fig. S8). The average Rg and RMSD values were 2.72 ± 0.45 and 4.03 ± 0.28 nm, respectively, attesting to the overall stability of the system throughout the simulation (Fig. 2E and 2F).

Statistical analysis of intermolecular hydrogen bonds in Fig. 2G yielded an average of 1.25 ± 1.02 per snapshot, suggesting a relatively minor contribution of hydrogen bonding to the overall assembly, consistent with the spectroscopic findings presented in Fig. 1F. The progressive reduction in centroid distance between BBR and Ce6, accompanied by increased contact frequency over the course of the simulation, further validates the self-assembly mechanism (Fig. S9 and S10). For comparison, MD simulations were also performed on BBR in the absence of Ce6 (Fig. S11). In this system, electrostatic repulsion between positively charged BBR molecules prevented their close approach and subsequent aggregation. Collectively, these computational results demonstrate rapid self-assembly between BBR and Ce6, driven predominantly by π-π stacking and modestly supported by hydrogen bonding.

2.3. Cellular uptake and mitochondria respiration inhibition

Leveraging the intrinsic fluorescence of BBR and Ce6, the cellular uptake of BBR-Ce6 NPs was investigated by confocal laser scanning microscopy (CLSM). HepG2 cells were incubated with free BBR, free Ce6, or BBR-Ce6 NPs for 1, 2, and 6 h. Under identical conditions, the nanoparticle-treated group exhibited markedly stronger red fluorescence than free Ce6 (Fig. 3A), indicating substantially enhanced intracellular delivery of the hydrophobic photosensitizer. These observations were further corroborated by flow cytometry and quantitative analyses (Fig. S12). Although cells exposed to free BBR displayed brighter green fluorescence than those treated with BBR-Ce6 NPs, co-assembly of BBR with Ce6 into a nano-system resulted in pronounced fluorescence attenuation (Fig. S13), attributable to fluorescence

resonance energy transfer (FRET) between the two chromophores within the nano-system. Consequently, green fluorescence intensity does not reliably reflect the cellular uptake efficiency of BBR in either molecular or nanoscale form. Nevertheless, quantitative determination of intracellular BBR by HPLC revealed significantly higher internalization efficiency for BBR-Ce6 NPs compared to free BBR (Fig. S14). These findings demonstrated that the supramolecular nanoplatform simultaneously enhanced the cellular uptake of two drugs.

The positive charge on the isoquinoline moiety of berberine confers inherent mitochondrial tropism, prompting investigation into the subcellular distribution of BBR-Ce6 NPs. Substantial overlap between the green fluorescence of BBR and the orange fluorescence of the mitochondrial probe (Fig. S15 and S16) confirmed effective mitochondrial targeting. Consistency between the trends in green and orange fluorescence intensities (Fig. 3B and S17) further indicated that nano-system construction does not compromise the mitochondrial localization capability of BBR. These results revealed that supramolecular self-assembly markedly enhances the internalization of both therapeutic agents while preserving the mitochondrial targeting function of BBR, thereby establishing a foundation for subsequent synergistic therapeutic effects.

Previous studies have reported that BBR suppresses OXPHOS through inhibition of mitochondrial respiratory chain complex I, thereby alleviating the hypoxic tumor microenvironment via reduced oxygen consumption (Fig. 3C). To validate this mechanism, HepG2 cells were exposed to PBS, free Ce6, free BBR, or BBR-Ce6 NPs, and mitochondrial complex I activity was subsequently quantified using a commercial assay kit. BBR treatment elicited a significant reduction in complex I activity (Fig. 3D); notably, this inhibitory effect was further amplified in cells treated with BBR-Ce6 NPs, an enhancement ascribed to the superior intracellular delivery efficiency of the nanomedicine. The impact of BBR-Ce6 NPs on mitochondrial respiration was further evaluated by measuring the oxygen consumption rate (OCR) with a Seahorse XFe96 analyzer. Whereas free Ce6 exerted negligible effects on OCR and free BBR produced only moderate suppression, BBR-Ce6 NPs-treated cells consistently exhibited the lowest OCR throughout the measurement period (Fig. 3E), indicating that nano-system self-assembly substantially potentiates BBR-mediated inhibition of oxidative phosphorylation. Quantitative analysis revealed the lowest basal and maximal respiration rates in the BBR-Ce6 NPs group, confirming potent suppression of mitochondrial respiration (Fig. 3F and 3G). ATP production was also substantially diminished in this group (Fig. 3H). Furthermore, the markedly reduced spare respiratory capacity observed following nanoparticle treatment reflects compromised mitochondrial adaptability of cancer cells to exogenous stress (Fig. 3I). These data collectively demonstrated that nanoscale self-assembly enhanced BBR internalization and markedly inhibits mitochondrial complex I activity within the electron transport chain (ETC), thereby disrupting oxidative phosphorylation and ultimately attenuating oxygen consumption.

2.4. ROS production and mitochondrial membrane potential assay

Motivated by the enhanced drug internalization and marked reduction in oxygen consumption, the PDT efficacy of BBR-Ce6 NPs was evaluated under normoxic and hypoxic conditions using DCFH-DA as a ROS indicator. Under normoxic conditions, HepG2 cells treated with BBR or BBR-Ce6 NPs showed negligible green fluorescence, whereas those subjected to Ce6 + laser or Ce6 + BBR+laser displayed substantial green fluorescence (Fig. 4A). Notably, the BBR-Ce6 NPs+laser group elicited the strongest fluorescence intensity across all groups. Conversely, hypoxic conditions markedly attenuated ROS generation in Ce6 + laser group. However, BBR supplementation substantially enhanced green fluorescence intensity, indicating that BBR-mediated suppression of mitochondrial respiration effectively alleviated tumor hypoxia. Furthermore, cells treated with BBR-Ce6 NPs produced even brighter green fluorescence, attributable to the concomitant enhancement of cellular uptake for both therapeutic components. Flow cytometric quantification of intracellular fluorescence intensity corroborated these observations (Fig. S18 and S19). Under normoxic conditions, Ce6 with laser irradiation elevated mean fluorescence intensity 3.7-fold relative to the PBS ; under hypoxic conditions, this enhancement diminished to only 2.1-fold. By contrast, BBR+Ce6 + laser group yielded 4.1-fold and 4.7-fold increases under normoxic and hypoxic conditions, respectively (Fig. 4B and 4C). This marked disparity indicated that BBR supplementation significantly potentiates photosensitizer-mediated ROS generation under hypoxic conditions. Remarkably, BBR-Ce6 NPs+laser group produced comparable enhancement factors under both oxygenation states (8.0-fold under normoxia and 6.2-fold under hypoxia), demonstrating robust ROS generation capacity even in hypoxic environments.

Mitochondrial membrane potential was subsequently evaluated using the JC-1 probe, wherein a shift from red to green fluorescence signifies membrane depolarization. As shown in Fig. 4D and 4E, under normoxic conditions, Ce6 + laser group exhibited discernible green fluorescence, whereas this signal was markedly attenuated under hypoxic conditions. Strikingly, BBR-Ce6 NPs+laser group displayed intense green fluorescence concomitant with diminished red fluorescence under both oxygenation states, indicating the most pronounced mitochondrial depolarization. Flow cytometric quantification across various treatment conditions produced results consistent with confocal observations (Fig. S20, S21, 4F and 4G). Taken together, these results position BBR-Ce6 NPs as a compelling therapeutic modality for PDT of oxygen-deprived tumors.

2.5. In vitro antitumor effect

The PDT efficacy of BBR-Ce6 NPs against HepG2 cells in vitro was evaluated using the CCK-8 assay. As shown in Fig. 5A and 5B, Ce6 exhibited minimal dark toxicity under both normoxic and hypoxic conditions, confirming its suitability as a photosensitizer for PDT. Despite enhancing intracellular BBR accumulation to a moderate extent, BBR-Ce6 NPs displayed limited cytotoxicity in the dark at the tested concentrations. Under normoxic conditions, laser irradiation markedly reduced the viability of Ce6-treated cells, while the physical mixture of BBR, Ce6, and laser irradiation failed to elicit additional cytotoxicity. By contrast, BBR-Ce6 NPs+laser exhibited the most pronounced cytotoxic effect, an outcome attributable primarily to the enhanced cellular internalization conferred by the nanoplatform. Under hypoxic conditions, Ce6-mediated photodynamic efficacy was substantially attenuated. Notably,

BBR supplementation partially restored this therapeutic effect. Remarkably, laser-irradiated BBR-Ce6 NPs retained potent antitumor performance activity even under hypoxic conditions. This pronounced potentiation stems from both enhanced intracellular delivery and BBR-driven alleviation of hypoxia via suppression of oxidative phosphorylation.

These findings were corroborated by Annexin V-FITC/PI staining (Fig. 5C and 5D). Under normoxic conditions with laser irradiation, apoptosis rates were 58.5% for Ce6-treated cells and 65.4% for cells receiving combined BBR and Ce6 treatment, whereas BBR-Ce6 NPs+laser induced the highest apoptosis rate (75.3%). Under hypoxic conditions, the viable cell proportion in the Ce6 + laser group was still as high as 79.8%. However, BBR supplementation in the Ce6 system or self-assembly into BBR-Ce6 NPs sharply reduced viable cell proportions to 48.4% and 32.4%, respectively. The antitumor efficacy was further visualized by live/dead staining via confocal laser scanning microscopy (Fig. 5E and 5F). Under both oxygenation states (normoxic and hypoxic), cells exposed to BBR-Ce6 NPs+laser displayed more intense red fluorescence (indicative of dead cells) than those treated with Ce6 + laser. In aggregate, the potent antitumor photodynamic efficacy of self-assembled BBR-Ce6 NPs under hypoxic conditions arises from enhanced cellular internalization coupled with BBR-mediated oxygen conservation.

2.6. In vivo antitumor study

Assessment of the biodistribution profile constitutes a prerequisite for evaluating the in vivo antitumor efficacy of nanomedicines. Once tumor volumes in HepG2 tumor-bearing mice reached approximately 200–300 mm^3, free Ce6 and BBR-Ce6 NPs were administered intravenously, with fluorescence images acquired at predetermined intervals (0, 1, 2, 6, 8 and12 h) post-injection. In the BBR-Ce6 NPs group, tumor-associated fluorescence intensified progressively over time, reaching a maximum at 6 h (Fig. 6A). By contrast, mice receiving free Ce6 displayed faint fluorescence at 2 h, followed by rapid attenuation. Ex vivo fluorescence imaging and quantitative analyses corroborated these observations (Fig. 6B and 6C), consistent with effective accumulation of BBR-Ce6 NPs in the tumor region via the EPR effect. The obtained data pinpoint the appropriate window for timing the follow-up laser treatment.

Building upon the superior in vitro cytotoxicity and efficient in vivo tumor accumulation, the in vivo antitumor efficacy of BBR-Ce6 NPs was subsequently investigated. Upon reaching approximately 100 mm^3, HepG2 tumor-bearing mice were randomly allocated to six treatment groups: PBS, BBR, BBR-Ce6 NPs, Ce6 + laser, BBR+Ce6 + laser, or BBR-Ce6 NPs+laser. The therapeutic regimen is schematically depicted in Fig. 6D, with tumor volume and body weight recorded every two days. The BBR group displayed modest tumor-suppressive property relative to the control (Fig. 6E). Formulation into BBR-Ce6 NPs conferred a moderate therapeutic enhancement. Under laser irradiation, both Ce6 and the BBR/Ce6 physical mixture produced comparable, moderate tumor inhibition. By contrast, BBR-Ce6 NPs+laser exhibited the most potent tumor suppression, an effect attributable to enhanced co-delivery of both agents via self-assembly, concomitant with BBR-mediated alleviation of tumor hypoxia, thereby potentiating photodynamic efficacy. Post-treatment, excised tumors were photographed and weighed, yielding results consistent with the tumor growth profiles (Fig. 6F and 6G). Notably, BBR-Ce6 NPs+laser

significantly prolonged survival in the HepG2 tumor-bearing mouse model (Fig. 6H). Therapeutic efficacy was further validated by hematoxylin and eosin (H&E) and TUNEL staining. Relative to all other groups, the BBR-Ce6 NPs+laser group displayed the most pronounced necrosis and apoptosis (Fig. 6I). Body weights increased progressively across all groups throughout the treatment course (Fig. 6J). Furthermore, histological examination of major organs by H&E staining revealed no morphological abnormalities in any group (Fig. S22). In combination, the present results indicated that BBR-Ce6 NPs formed via self-assembly exert robust antitumor potency whilst preserving acceptable systemic biocompatibility.

3. Conclusion

In summary, we successfully developed a carrier-free self-assembly nanodrug BBR-Ce6 NPs, composed of the mitochondria-targeting OXPHOS inhibitor BBR and the photosensitizer Ce6 to enhance PDT through sustained alleviation of tumor hypoxia. Both experimental characterization and molecular dynamics simulations demonstrated that the self-assembly of BBR and Ce6 was predominantly driven by π–π stacking interactions and hydrogen bonding, resulting in structurally stable nanoparticles with high drug-loading efficiency. The nanodrug also showed enhanced cellular uptake and efficient tumor accumulation following systemic administration. Notably, after intracellular release of BBR-Ce6 NPs, BBR preferentially accumulated in mitochondria and effectively inhibited mitochondrial complex I, thereby suppressing OXPHOS and markedly reducing cellular oxygen consumption. Through this oxygen-conserving mechanism, BBR-Ce6 NPs achieved sustained alleviation of tumor hypoxia, significantly enhancing ROS generation and PDT efficacy under hypoxic conditions both in vitro and in vivo. Unlike conventional oxygen-delivery strategies that provide only transient oxygen replenishment, this metabolic regulation strategy improves PDT performance by persistently reducing oxygen consumption within the hypoxic tumor microenvironment. Furthermore, the carrier-free design avoids the use of inert excipients, enabling high drug-loading efficiency while minimizing potential carrier-associated toxicity and simplifying nanoparticle fabrication. Overall, this study presents a mitochondria-targeted and oxygen-economizing nanoplatform that effectively overcomes hypoxia-induced limitations in PDT by reducing tumor oxygen consumption. In addition, the carrier-free self-assembly strategy not only improves therapeutic precision and photodynamic efficacy, but also offers a simple, biocompatible, and highly efficient approach for constructing multifunctional nanomedicines. These findings provide a promising framework for the rational design of supramolecular self-assembled therapeutics aimed at enhancing the treatment of hypoxic solid tumors.

4. Experimental Section

4.1. Preparation and characterization of BBR-Ce6 NPs

BBR-Ce6 NPs were prepared using a nanoprecipitation method. Ce6 and BBR were individually dissolved in tetrahydrofuran and methanol, respectively, and then mixed at a 1:1 (w/w) ratio. The pH of the resulting solution was adjusted to 7.5 using 0.1 M NaOH. Under continuous stirring at 60°C and 1000

rpm, the organic phase was introduced dropwise at 1 mL/min via a micro-syringe pump into 5 mL of pre-warmed PBS (pH 7.4). Stirring was maintained for 12 h to facilitate nanoparticle self-assembly and evaporation of organic solvents. The crude dispersion was then transferred into a dialysis bag (MWCO 3000 Da) and dialyzed against deionized water for 24 h, with water replenished every 6 h, to eliminate free drugs and residual solvents. Following dialysis, the dispersion was stored at 4°C in the dark. The hydrodynamic diameter and zeta potential were determined by dynamic light scattering (DLS), while morphology was examined using transmission electron microscopy (TEM).

4.2. In Vitro drug release study

The pH-dependent drug release profile of the nanoparticles was evaluated using a dynamic dialysis technique. Briefly, 2 mL of BBR-Ce6 NPs dispersion was loaded into a dialysis bag (MWCO 3000 Da) and immersed in 28 mL of PBS release medium (supplemented with 0.5% Tween 80), which was adjusted to either pH 5.0 (to mimic the tumor microenvironment) or pH 7.4 (simulating physiological conditions). The setup was then agitated at 37°C and 180 rpm. At predetermined intervals, 2 mL of the external medium was withdrawn and replaced with an equal volume of fresh medium. The cumulative release curve of each drug was determined by quantifying the concentrations of Ce6 and BBR in the collected samples using UV-vis absorption spectroscopy and high-performance liquid chromatography (HPLC), respectively.

4.3. Singlet oxygen ($^1O_2$) generation detection

The generation $^1O_2$ was detected using the Singlet Oxygen Sensor Green (SOSG) fluorescent probe. The experimental setup included the following groups: (A) PBS + SOSG; (B) free Ce6 (2 μg/mL) + SOSG; (C) BBR-Ce6 NPs (Ce6 equivalent concentration: 2 μg/mL) + SOSG. The final concentration of SOSG was 5 μM. Samples were irradiated using a 660 nm laser (50 mW/cm²) for 5 min. Fluorescence intensity was measured at 1-min intervals (excitation/emission: 488/520 nm) with a fluorescence spectrometer. The amount of $^1O_2$ produced was expressed as ΔFI (FI / FI_0).

4.4. Molecular dynamic simulation

Molecular dynamics simulations were performed using the following protocol. Initially, molecular modeling of small molecules was carried out with Chem3D, followed by structural energy minimization employing the MM2 force field. The small molecules were subsequently parameterized using the CGenFF program, with the Berberine molecule assigned a formal positive charge. All simulations were conducted using Gromacs 2025.1 under the Charmm36 force field. A cubic simulation box of 8 × 8 × 8 nm³ was constructed, and 20 molecules each of berberine and Ce6 were placed inside. Periodic boundary conditions (PBC) were applied in all directions. The system was solvated with TIP3P water molecules, resulting in the addition of 16,024 water molecules to fill the remaining volume. Chloride ions were introduced to neutralize the overall charge of the system. Electrostatic interactions were treated using the Particle Mesh Ewald (PME) method, while the Verlet cut-off scheme was employed for neighbor searching. Both van der Waals and Coulombic interactions were computed with a cut-off distance of 1.0 nm. The system was then equilibrated sequentially under the canonical (NVT) ensemble

at 310 K and the isothermal-isobaric (NPT) ensemble at 1 atm pressure. Bonds involving hydrogen atoms were constrained using the LINCS algorithm to maintain structural stability. Following equilibration, a production molecular dynamics simulation was performed for 100 ns under the NPT ensemble, with an integration time step of 2 fs.

4.5. Cellular uptake and subcellular co-localization

HepG2 cells were seeded into confocal dishes at a density of 1×10^5 cells per well and cultured for 24 h to allow for adherence. Following this, the culture medium was replaced with fresh medium containing free Ce6, free BBR, or BBR-Ce6 NPs, and the cells were further incubated for 1, 2, or 6 h. Subsequently, the cells were washed with PBS and stained with 200 nM Mito-Tracker™ Red CMXRos working solution at 37°C in the dark for 30 min to label mitochondria. After staining, the cells were fixed with 4% paraformaldehyde for 15 min. Cellular imaging was performed using confocal microscopy with the following excitation/emission settings: BBR (Ex:405 nm; Em: 510–530 nm), Ce6 (Ex:634 nm; Em:660–700 nm), and Mito-Tracker Red (Ex:543 nm; Em:591–620 nm).

4.6. Mitochondrial complex I activity assay

To evaluate the inhibitory effect of BBR on mitochondrial Complex I, enzyme activity was measured using a commercial assay kit. HepG2 cells were seeded at a density of 2×10^5 cells per well. After 24 h of culture, the cells were treated for an additional 24 h with the following: (1) PBS (control), (2) Ce6 (2 μg/mL), (3) BBR (1.8 μg/mL), or (4) BBR-Ce6 NPs (BBR equivalent concentration: 1.8 μg/mL). Following treatment, cells were washed with ice-cold PBS, scraped, and mitochondrial extracts were isolated according to the kit protocol. The change in absorbance at 340 nm was recorded continuously for 10 min, and Complex I activity was calculated from the initial rate of NADH oxidation.

4.7. Oxygen consumption detection

Cellular energy metabolism was assessed in real time using a Seahorse XFe96 Analyzer. HepG2 cells were seeded in a Seahorse XFe96 cell culture microplate. Following 24 h of culture, the cells were treated for another 24 h with one of the following: PBS, Ce6 (2 μg/mL), BBR (1.8 μg/mL), or BBR-Ce6 NPs (BBR equivalent concentration: 1.8 μg/mL). One hour prior to the assay, the culture medium was replaced with pre-warmed Seahorse XF assay medium (pH 7.4), and the plate was incubated in a non-CO_2 incubator at 37°C for equilibration. During the assay, oligomycin (1.5 μM), FCCP (1.5 μM), and a mixture of rotenone/antimycin A (0.5 μM each) were sequentially injected according to the standard mitochondrial stress test protocol. Oxygen consumption rate (OCR) was monitored in real time, and key metabolic parameters, including basal respiration, ATP-linked respiration, maximal respiratory capacity, and spare respiratory capacity, were calculated from the resulting OCR profiles.

4.8. Intracellular ROS detection

HepG2 cells were seeded at a density of 1×10^5 cells per well and cultured overnight. The cells were then treated under either normoxic or hypoxic conditions with the following agents: (1) PBS, (2) BBR (1.8 μg/mL), (3) BBR-Ce6 NPs (BBR:1.8 μg/mL, Ce6:2.0 μg/mL) (4) Ce6 (2.0 μg/mL) + Laser, (5) BBR (1.8

μg/mL) + Ce6 (2.0 μg/mL) + Laser, or (6) BBR-Ce6 NPs (BBR:1.8 μg/mL, Ce6:2.0 μg/mL) + Laser. Following 24 h of drug incubation, the laser-treated groups were exposed to a 660 nm laser at a power density of 50 mW/cm² for 5 min. After treatment, the medium was removed, and the cells were washed with PBS. Subsequently, serum-free medium containing 5 μM DCFH-DA was added to load the fluorescent probe, and the cells were incubated at 37°C in the dark for 30 min. Following three washes with PBS, intracellular green fluorescence (excitation/emission: 488/525 nm) was immediately visualized using confocal microscopy. Additionally, the mean fluorescence intensity of the cells was quantified by flow cytometry. Normoxic culture was maintained at 21% O_2. For hypoxic conditions, cell plates were transferred into an anaerobic jar (O_2 <1%).

4.9. Mitochondrial membrane potential detection

Cell treatments were performed as described in the previous section. Following the manufacturer's protocol for the JC-1 assay, 1 mL of JC-1 staining working solution was added to each well. Cells were incubated at 37°C in the dark for 30 min and then washed twice with the supplied assay buffer. Mitochondrial membrane potential was assessed directly by confocal microscopy. JC-1 forms red-fluorescent aggregates (excitation/emission: 543/600 nm) in mitochondria with intact membrane potential, whereas it remains in a green-fluorescent monomeric state (excitation/emission: 488/530 nm) upon depolarization. Additionally, the red-to-green fluorescence intensity ratio was measured by flow cytometry to quantify the proportion of cells with diminished mitochondrial membrane potential.

4.10. Cytotoxicity evaluation

Cell viability was assessed using the CCK-8 assay. HepG2 cells in the logarithmic growth phase were seeded in 96-well plates at a density of 5×10³ cells per well. After overnight incubation, the cells were treated under either normoxic or hypoxic conditions with the following: (1) BBR, (2) Ce6, (3) BBR-Ce6 NPs, (4) Ce6 + Laser, (5) BBR + Ce6 + Laser, or (6) BBR-Ce6 NPs + Laser. Following 24 h of drug incubation, Laser irradiation was performed using the parameters (660 nm, 50 mW/cm², 5 min). The cells were then cultured for an additional 24 h, after which CCK-8 reagent was added and incubated for 4 h. Absorbance was measured at 450 nm to calculate cell viability.

4.11. Cell apoptosis analysis

HepG2 cells were seeded at a density of 2×10⁵ cells per well. After 24 h of culture, cells were treated for an additional 24 h with the designated reagents under either normoxic or hypoxic conditions. The treatment groups were as follows: (1) PBS, (2) BBR (1.8 μg/mL), (3) BBR-Ce6 NPs (BBR:1.8 μg/mL, Ce6:2.0 μg/mL) (4) Ce6 (2.0 μg/mL) + Laser, (5) BBR (1.8 μg/mL) + Ce6 (2.0 μg/mL) + Laser, or (6) BBR-Ce6 NPs (BBR:1.8 μg/mL, Ce6:2.0 μg/mL) + Laser. Laser irradiation (660 nm, 50 mW/cm²) was applied for 5 minutes to the designated groups immediately after the drug incubation period. Following treatment, all cells (including those in the supernatant) were collected, pooled, washed with PBS, and resuspended in 100 μL of 1× binding buffer. Cell suspensions were then stained by adding 5 μL of Annexin V-FITC and 10 μL of propidium iodide (PI), gently mixed, and incubated at room temperature in

the dark for 15 minutes. Finally, 400 μL of binding buffer was added to each sample prior to immediate acquisition on a flow cytometer.

4.12. Live/Dead cell staining

Cell harvesting and treatment protocols were identical to those described in the previous section. After being washed with PBS, cells were stained with 1 mL of a solution containing 2 μM Calcein-AM and 4 μM PI per well and incubated at 37°C in the dark for 30 min. Following a subsequent PBS wash, live/dead staining was visualized immediately using Confocal laser scanning microscope.

4.13. In Vivo biodistribution study

When tumor volume in tumor-bearing mice reached approximately 200 mm^3, mice were randomly divided into two groups (n = 3): (1) Ce6; (2) BBR-Ce6 NPs. Administration was via tail vein injection (Ce6: 3 mg/kg). At 0, 1, 2, 6, 8, and 12 h post-injection, mice were anesthetized, and fluorescence images were acquired using a small animal *in vivo* imaging system. Fluorescence intensity (units: p/s/cm^2/sr) was quantified using Living Image® software. At 12 h, mice were euthanized, major organs and tumors were harvested for *ex vivo* imaging.

4.14. Evaluation of anti-tumor efficacy in vivo

When the average tumor volume reached approximately 100 mm^3, a subset of mice was randomly allocated into six groups (n = 5):(G1) PBS, (G2) BBR (2.7 mg/kg), (G3) BBR-Ce6 NPs (BBR: 2.7 mg/kg, Ce6: 3.0 mg/kg) (G4) Ce6 (2.0 mg/kg) + Laser, (G5) BBR (2.7 mg/kg) + Ce6 (3.0 mg/kg) + Laser, or (G6) BBR-Ce6 NPs (BBR:2.7 mg/kg, Ce6: 3.0 mg/kg) + Laser. Treatments were administered via tail-vein injection every two days for a total of five doses. For groups G4 and G5, the tumor region was irradiated with a 660 nm laser (50 mW/cm^2) for 5 minutes at 2 h post-injection. For group G6, laser irradiation was performed 6 hours after administration. Tumor volume and body weight were recorded every two days. On day 21, mice were euthanized, tumors were excised, weighed, and photographed. Major organs were collected for histopathological examination by hematoxylin and eosin (H&E) staining. Tumor tissues were sectioned for H&E and TUNEL staining analyses. The remaining mice were maintained for 60 days to assess survival outcomes. Mice exhibiting moribund conditions or tumor volumes exceeding 2000 mm^3 were euthanized prior to the scheduled experimental endpoint.

Declarations

Declaration of Competing Interest

The authors declare that they have no known competing financial interests or personal relationships that could have appeared to influence the work reported in this paper.

Author Contribution

Xin Xie: Writing - original draft, Project administration, Funding acquisition, Conceptualization; Tao Quan: Project administration, Methodology, Investigation; Haiqian Zhang: Methodology, Validation, Investigation; Rui Liang: Investigation, Methodology, Funding acquisition, Validation; Yong Huang: Visualization, Methodology, Funding acquisition; Lihe Sun: Methodology, Funding acquisition, Formal analysis; Fengmin Xiu: Investigation, Validation; Biao Zheng: Formal analysis, Validation; Shangjun Zhou: Validation, Supervision, Writing - review & editing, Chaohui Zhen: Validation, Supervision, Funding acquisition, Xinsheng Peng: Validation, Supervision, Writing - review & editing; Bowen Li: Writing - review & editing, Supervision, Conceptualization. All authors read and approved the final manuscript.

Acknowledgments:

This work was supported by the National Natural Science Foundation of China (32101129, 32501251), Guangdong Basic and Applied Basic Research Foundation (2024A1515140042, 2023A1515110324), Medical Scientific Research Foundation of Guangdong Province (A2025169, A2024591), Clinical & Basic Science Technology Innovation Project of Guangdong Medical University (GDMULCJC2024101, GDMULCJC2025239), Talent Development Foundation of The First Dongguan Affiliated Hospital of Guangdong Medical University (GCC2023016, GCC2025013), Dongguan Science and Technology of Social Development Program (20231800940202, 20231800937512).

Data availability

Data will be made available on request.

References

1. Vellingiri Y, Yu B, Cong H. Recent developments in nanomedicine-integrated photodynamic therapy for cancer. Coord Chem Rev. 2026;548:217170. https://doi.org/10.1016/j.ccr.2025.217170.
2. Alhoussein J, Merabishvili K, Ho T, Elkihel A, Cressey P, Tóth Á, Qian A, Hery M, Vergnaud J, Domenichini S, Di Meo F, Chen J, Zheng G, Makky A. Next generation of porphysomes for improved photodynamic therapy applications. J Controlled Release. 2025;381:113621. https://doi.org/10.1016/j.jconrel.2025.113621.
3. Chen H, Wang Y, He Z, Wan Y, Cao C, Lu Z, Gao Y, Cui X, Lee KW, Tan JH, Xu W, Yang Y, Li X, Wang Y, Hou J, Li S, Lee CS. De Novo Design of Efficient NIR-II-Activated Heavy-Atom-Free Type-I Photosensitizer for Anti-Tumor Photoimmunotherapy. Adv Mater. 2025;37:2501919. https://doi.org/10.1002/adma.202501919.
4. Zhang J, Jiao D, Qi X, Zhang Y, Liu X, Pan T, Gao H, Liu Z, Ding D, Feng G. An Albumin-Photosensitizer Supramolecular Assembly with Type I ROS-Induced Multifaceted Tumor Cell Deaths for Photodynamic Immunotherapy. Adv Sci. 2025;12:2410405. https://doi.org/10.1002/advs.202410405.

5. Li Y, Li Y, He G, Li X, Ding R, Yan R, Lin J, Huang P. Activatable Enzymatic Nanoplatform Incorporated into Microneedle Patch for Relieving Tumor Hypoxia Augmented Photodynamic Therapy. Adv Mater. 2025;37:2504258. https://doi.org/10.1002/adma.202504258.
6. Bhardwaj A, Panepinto MC, Ueberheide B, Neel BG. A mechanism for hypoxia-induced inflammatory cell death in cancer. Nature. 2024;637:470–7. https://doi.org/10.1038/s41586-024-08136-y.
7. Roque JA, Barrett PC, Cole HD, Lifshits LM, Shi G, Monro S, von Dohlen D, Kim S, Russo N, Deep G, Cameron CG, Alberto ME, McFarland SA. Breaking the barrier: an osmium photosensitizer with unprecedented hypoxic phototoxicity for real world photodynamic therapy. Chem Sci. 2020;11:9784–806. https://doi.org/10.1039/d0sc03008b.
8. Cole HD, Roque JA, Shi G, Lifshits LM, Ramasamy E, Barrett PC, Hodges RO, Cameron CG, McFarland SA. Anticancer Agent with Inexplicable Potency in Extreme Hypoxia: Characterizing a Light-Triggered Ruthenium Ubertoxin. J Am Chem Soc. 2021;144:9543–7. https://doi.org/10.1021/jacs.1c09010.
9. Yang F, Chen F, Li S, Wang S, Peng L, Deng S, Zhang F, Jeschke U, Wang Y, Luo C. Emerging tumor hypoxia-relieving nanotherapeutics for boosting photodynamic therapy. Chem Eng J. 2025;516:163962. https://doi.org/10.1016/j.cej.2025.163962.
10. Song Y, Gu Y, Lei Z, Li N, Zhang Y, Yu Q, Liu Y. Fluorinated Cyclodextrin Supramolecular Nanoassembly Enables Oxygen-Enriched and Targeted Photodynamic Therapy. Nano Lett. 2025;25:4476–84. https://doi.org/10.1021/acs.nanolett.5c00090.
11. Mohanto N, Mondal H, Park YJ, Jee JP. Therapeutic delivery of oxygen using artificial oxygen carriers demonstrates the possibility of treating a wide range of diseases. J Nanobiotechnol. 2025;23:25. https://doi.org/10.1186/s12951-024-03060-9.
12. Day RA, Sletten EM. Perfluorocarbon nanomaterials for photodynamic therapy. Curr Opin Colloid in. 2021;54:101454. https://doi.org/10.1016/j.cocis.2021.101454.
13. Chen S, Fan J, Xie Q, Qin Y, Xie H, Xiao C, Wang W, Liu B. Bufotalin loaded biomimetic nanodrug for combined chemo/photodynamic therapy of cancer. Mater Today Bio. 2025;32:101684. https://doi.org/10.1016/j.mtbio.2025.101684.
14. Alizadeh N, Salimi A, Sham T-K, Bazylewski P, Fanchini G, Fathi F, Soleimani F. Hierarchical $Co(OH)_2$/FeOOH/WO_3 ternary nanoflowers as a dual-function enzyme with pH-switchable peroxidase and catalase mimic activities for cancer cell detection and enhanced photodynamic therapy. Chem Eng J. 2021;417:129134. https://doi.org/10.1016/j.cej.2021.129134.
15. Moloudi K, Abrahamse H, George BP. Nanotechnology-mediated photodynamic therapy: Focus on overcoming tumor hypoxia, WIREs Nanomed. Nanobi. 16 (2023) e1937. https://doi.org/10.1002/wnan.1937
16. Wang T, Liu T, Li Z, Wu D, Zhao X, Zeng L. Ultrasmall gold-encapsulated mesoporous platinum to promote photodynamic/catalytic therapy through cascade enzyme-like reactions. J Colloid Interface Sci. 2025;680:117–28. https://doi.org/10.1016/j.jcis.2024.11.008.

17. Lei L, Dai W, Zhao J, Jiang A, Peng H, Jin Q, Li X, Tang Z. A pH-Sensitive Nanosized Covalent-Organic Polymer for Enhanced Tumor Photodynamic Immunotherapy by Hypoxia Relief and STAT3 Inhibition. Adv Sci. 2025;12:2504860. https://doi.org/10.1002/advs.202504860.
18. Zhang Z, Zhao Q, Xu Q, Deng Q, Hua A, Wang X, Yang X, Li Z. A mitochondria-interfering nanocomplex cooperates with photodynamic therapy to boost antitumor immunity. Biomaterials. 2025;317:123094. https://doi.org/10.1016/j.biomaterials.2025.123094.
19. Bartusik-Aebisher D, Saad MA, Przygórzewska A, Woźnicki P, Aebisher D. Latest Nanoparticles to Modulate Hypoxic Microenvironment in Photodynamic Therapy of Cervical Cancer: A Review of In Vivo Studies. Int J Mol Sci. 2025;26:8503. https://doi.org/10.3390/ijms26178503.
20. Zhou Q, Shubhra QTH, Lai P, Shi J, Fang C, Guo Q, Li W, Chen R, Shen X, Huang L, Cai X, Lin S. Genistein and chlorin E6-loaded versatile nanoformulation for remodeling the hypoxia-related tumor microenvironment and boosting photodynamic therapy in nasopharyngeal carcinoma treatment. Adv Compos Hybrid Mater. 2025;8:145. https://doi.org/10.1007/s42114-024-01158-0.
21. Li M, Shao Y, Kim JH, Pu Z, Zhao X, Huang H, Xiong T, Kang Y, Li G, Shao K, Fan J, Foley JW, Kim JS, Peng X. Unimolecular Photodynamic O2-Economizer To Overcome Hypoxia Resistance in Phototherapeutics. J Am Chem Soc. 2020;142:5380–8. https://doi.org/10.1021/jacs.0c00734.
22. Li S, Yang F, Wang Y, Jia L, Hou X. Self-reported and self-facilitated theranostic oxygen nano-economizer for precise and hypoxia alleviation-potentiated photodynamic therapy. Mater Horiz. 2023;10:5734–52. https://doi.org/10.1039/d3mh01244a.
23. Wang K, Wang F, Yu M, Huang Y, Zhou Q, Lai W, Huang R, Xu T, Xie D, Wang Z, Wu J, Cai K, Huang J. Cascade-targeting oxygen-self-supplying nano-photosensitizer for enhanced photodynamic immunotherapy of triple-negative breast cancer. Acta Biomater. 2026;215:254–71. https://doi.org/10.1016/j.actbio.2026.03.038.
24. Yang F, Li S, Ji Q, Zhang H, Zhou M, Wang Y, Zhang S, Sun J, He Z, Luo C. Modular Prodrug-Engineered Oxygen Nano-Tank With Outstanding Nanoassembly Performance, High Oxygen Loading, and Closed-Loop Tumor Hypoxia Relief. Adv Sci. 2024;11:2405583. https://doi.org/10.1002/advs.202405583.
25. Bai Z, Guo L, Huang J, Li H, An G, Zheng H, Wang N, Li Z, Zhu Y. Biomimetic metal organic frameworks mediated by metformin and 1-MT for enhancing the synergistic treatment of photodynamic therapy, photothermal therapy and immunotherapy. Chem Eng J. 2024;479:147932. https://doi.org/10.1016/j.cej.2023.147932.
26. Chen D, Suo M, Guo J, Tang W, Jiang W, Liu Y, Duo Y. Development of MOF Armor-Plated Phycocyanin and Synergistic Inhibition of Cellular Respiration for Hypoxic Photodynamic Therapy in Patient-Derived Xenograft Models. Adv Healthc Mater. 2020;10:2001577. https://doi.org/10.1002/adhm.202001577.
27. Yuan P, Deng FA, Liu YB, Zheng RR, Rao XN, Qiu XZ, Zhang DW, Yu XY, Cheng H, Li SY. Mitochondria Targeted O_2 Economizer to Alleviate Tumor Hypoxia for Enhanced Photodynamic Therapy. Adv Healthc Mater. 2021;10:2100198. https://doi.org/10.1002/adhm.202100198.

28. Beerkens APM, Heskamp S, Reinema FV, Adema GJ, Span PN, Bussink J. Mitochondria Targeting of Oxidative Phosphorylation Inhibitors to Alleviate Hypoxia and Enhance Anticancer Treatment Efficacy, Clin. Cancer Res. 2025;31:1186–93. https://doi.org/10.1158/1078-0432.ccr-24-3296.
29. Li Z, Wang Y, Xu Q, Ma J, Li X, Yan J, Tian Y, Wen Y, Chen T. Berberine and health outcomes: An umbrella review. Phytother Res. 2023;37:2051–66. https://doi.org/10.1002/ptr.7806.
30. Zheng X, Zhao Y, Jia Y, Shao D, Zhang F, Sun M, Dawulieti J, Hu H, Cui L, Pan Y, Yang C, Sun W, Zhang S, He K, Li J, Du J, Zhang M, Chen L. Biomimetic co-assembled nanodrug of doxorubicin and berberine suppresses chemotherapy-exacerbated breast cancer metastasis. Biomaterials. 2021;271:120716. https://doi.org/10.1016/j.biomaterials.2021.120716.
31. Cheng Y, Ji Y. Mitochondria-targeting nanomedicine self-assembled from GSH-responsive paclitaxel-ss-berberine conjugate for synergetic cancer treatment with enhanced cytotoxicity. J Controlled Release. 2020;318:38–49. https://doi.org/10.1016/j.jconrel.2019.12.011.
32. Turner N, Li JY, Gosby A, To SWC, Cheng Z, Miyoshi H, Taketo MM, Cooney GJ, Kraegen EW, James DE, Hu LH, Li J, Ye JM, Diabetes. 57 (2008) 1414–8, https://doi.org/10.2337/db07-1552
33. Zheng C, Luo W, Liu Y, Chen J, Deng H, Zhou Z, Shen J. Killing three birds with one stone: Multi-stage metabolic regulation mediated by clinically usable berberine liposome to overcome photodynamic immunotherapy resistance. Chem Eng J. 2023;454:140164. https://doi.org/10.1016/j.cej.2022.140164.
34. Ma X, Han Y, Liu K, Bai Y, Gao H, Hou Y, Bai G. Chemical proteomics combined with metabonomics reveals berberine targets NDUFV1 of complex I in the respiratory chain to regulate energy metabolism. Chin Chem Lett. 2023;34:107595. https://doi.org/10.1016/j.cclet.2022.06.018.
35. Sun J, Ye T, Chen X, Li B, Wei Y, Zheng H, Piao J, Li F. A self-assembly active nanomodulator based on berberine for photothermal immunotherapy of breast cancer via dual regulation of immune suppression. Int J Pharm. 2024;653:123898. https://doi.org/10.1016/j.ijpharm.2024.123898.
36. Guo X, Luo W, Wu L, Zhang L, Chen Y, Li T, Li H, Zhang W, Liu Y, Zheng J, Wang Y. Natural Products from Herbal Medicine Self-Assemble into Advanced Bioactive Materials. Adv Sci. 2024;11:2403388. https://doi.org/10.1002/advs.202403388.
37. Karaosmanoglu S, Zhou M, Shi B, Zhang X, Williams GR, Chen X. Carrier-free nanodrugs for safe and effective cancer treatment. J Controlled Release. 2021;329:805–32. https://doi.org/10.1016/j.jconrel.2020.10.014.
38. Xu Y, Yang L, Wang C, Sun W, Zheng Y, Ou B, Wu L, Shi L, Lin X, Chen W. Ferroptosis boosted oral cancer photodynamic therapy by carrier-free Sorafenib-Ce6 self-assembly nanoparticles. J Controlled Release. 2024;366:798–811. https://doi.org/10.1016/j.jconrel.2023.12.056.
39. Seo M, Jeong YH, Seo B, Han SK, Yang SB, Lee JH, Lee JH, Ma G, Park ES, Choi JU, Park J. Lenalidomide-utilizing self-assembled immunogenic cell death-inducing heparin/doxorubicin nanocomplex for anticancer immunotherapy. Nano Today. 2025;62:102677. https://doi.org/10.1016/j.nantod.2025.102677.

40. Lu Z, Wang T, Xu X, Hu Q, Wang L, Jin Y. Carrier-free nano-integrated strategy of phototherapy and chemotherapy for synergetic AKT targeted therapy to inhibit cancer metastasis and recurrence. J Nanobiotechnol. 2025;23:520. https://doi.org/10.1186/s12951-025-03539-z.
41. Shim MK, Yang S, Park J, Yoon JS, Kim J, Moon Y, Shim N, Jo M, Choi Y, Kim K. Preclinical development of carrier-free prodrug nanoparticles for enhanced antitumor therapeutic potential with less toxicity. J Nanobiotechnol. 2022;20:436. https://doi.org/10.1186/s12951-022-01644-x.
42. Li G, Lu M, Jiao Z, Zheng S, Xiao H, Li M, Shi J, Liu X, He Z, Sun B, Sun J. Structural Topology of Prodrug Nanoassembly: First Steps Toward Nano-QSAR. Adv Funct Mater. 2026;14. https://doi.org/10.100/adfm.755152.
43. Cui J, Xue Z, Zhang Z, Zhu H, Miao M, Song Y, Li X, Zeng H, Wu X. GSH-Triggered Self-Cascading Nanoreactor Integrates Efficient ICD Induction and Immune Checkpoint Blockade for Pancreatic Cancer Therapy. Adv Funct Mater. 2025;36:2520855. https://doi.org/10.1002/adfm.202520855.
44. Wang J, Dong W, Zhang J, Liu L, Ji P, Yuan X, Shuang S, Fu D, Guo Z, Tian Y, Shen R, Wang D. Hypoxia-Responsive Nanosystem for Synergistic Cancer Therapy: Enhancing Ferroptosis via a Novel GPX4 Inhibitor and Facilitating Precise Photodynamic Therapy. Adv Funct Mater. 2026;36:e29287. https://doi.org/10.1002/adfm.202529287.
45. Chen S, Chen Z, Wang Y, Hao W, Yuan Q, Zhou H, Gao C, Wang Y, Wu X, Wang S. Targeted delivery of Chinese herb pair-based berberine/tannin acid self-assemblies for the treatment of ulcerative colitis. J Adv Res. 2022;40:263–76. https://doi.org/10.1016/j.jare.2021.11.017.
46. Gao S, Zheng H, Xu S, Kong J, Gao F, Wang Z, Li Y, Dai Z, Jiang X, Ding X, Lei H. Novel Natural Carrier-Free Self-Assembled Nanoparticles for Treatment of Ulcerative Colitis by Balancing Immune Microenvironment and Intestinal Barrier. Adv Healthc Mater. 2023;12:2301826. https://doi.org/10.1002/adhm.202301826.
47. Mai Z, Zhong J, Zhang J, Chen G, Tang Y, Ma W, Li G, Feng Z, Li F, Liang X-J, Yang Y, Yu Z. Carrier-Free Immunotherapeutic Nano-Booster with Dual Synergistic Effects Based on Glutaminase Inhibition Combined with Photodynamic Therapy. ACS Nano. 2023;17:1583–96. https://doi.org/10.1021/acsnano.2c11037.
48. Huang JQ, Zhao LP, Zhou X, Liu LS, Zheng RR, Deng FA, Liu YB, Yu XY, Li SY, Cheng H. Carrier Free O_2-Economizer for Photodynamic Therapy Against Hypoxic Tumor by Inhibiting Cell Respiration. Small. 2022;18:2107467. https://doi.org/10.1002/smll.202107467.
49. Su Q, Wang Z, Zhou H, Zhang M, Deng W, Wei X, Xiao J, Duan X. Eradication of Large Tumors by Nanoscale Drug Self-Assembly. Adv Mater. 2024;36:2410536. https://doi.org/10.1002/adma.202410536.
50. Yu BX, Liu YB, Chen XY, Zhang W, Cen Y, Yan MY, Liu QQ, Li SY. Self-Assembled PD-L1 Downregulator to Boost Photodynamic Activated Tumor Immunotherapy Through CDK5 Inhibition. Small. 2024;20:2311507. https://doi.org/10.1002/smll.202311507.
51. Huang CY, Zhao LP, Rao XN, Zheng RR, Liu ZS, Cai H, Zhang W, Chen AL, Xu L, Li S. Chlorin e6 and BLZ945 Based Self-Assembly for Photodynamic Immunotherapy Through Immunogenic Tumor

Induction and Tumor-Associated Macrophage Depletion. Adv Healthc Mater. 2024;13:2304576. https://doi.org/10.1002/adhm.202304576.

52. Qu H, Chen H, Cheng W, Wang Y, Xia Y, Zhang L, Ma B, Hu R, Xue X. A supramolecular assembly strategy for hydrophilic drug delivery towards synergistic cancer treatment. Acta Biomater. 2023;164:407–21. https://doi.org/10.1016/j.actbio.2023.04.026.

Scheme 1

Scheme 1 is available in the Supplementary Files section.

Figures

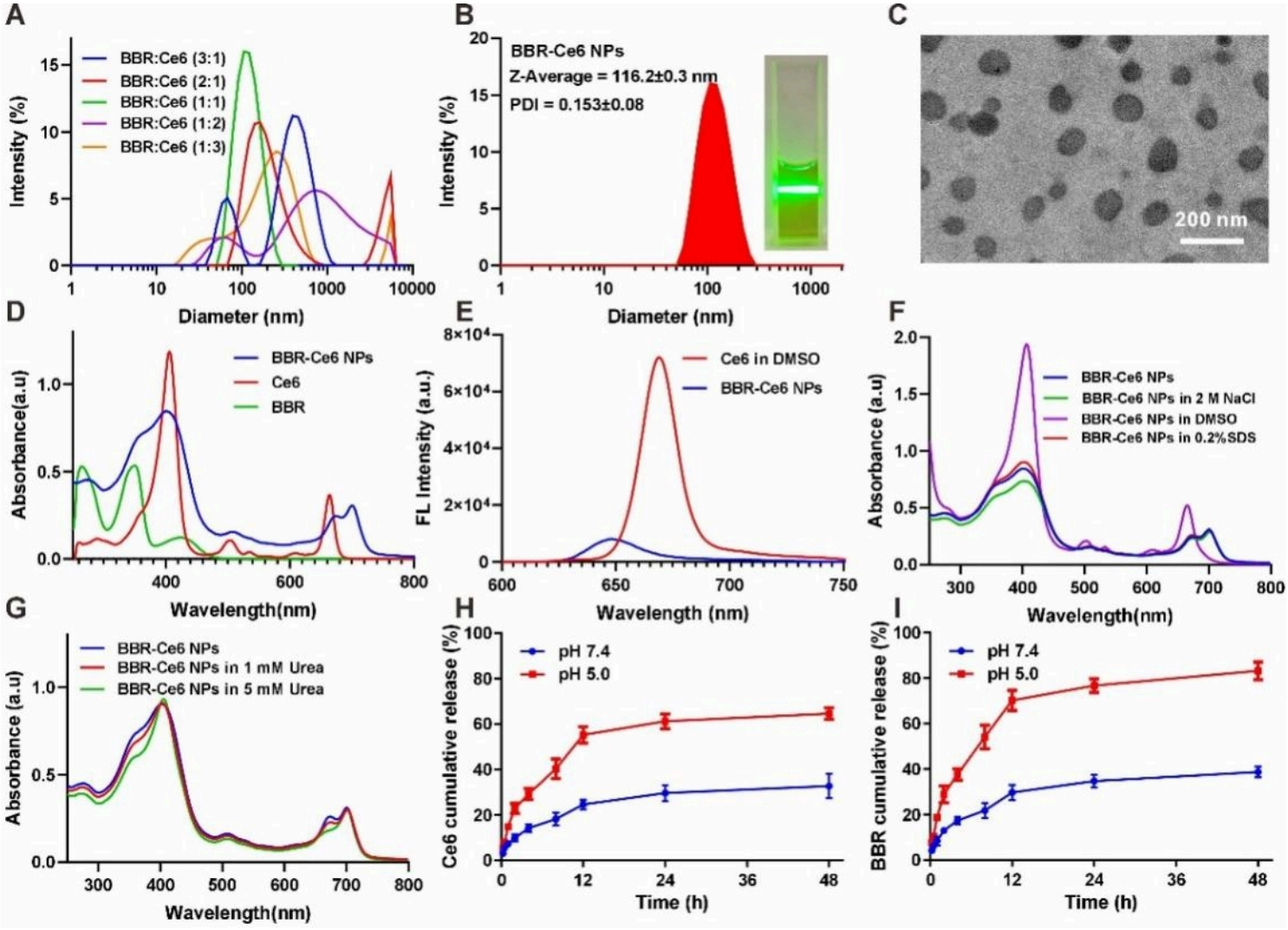


Figure 1

Characterization of BBR-Ce6 NPs(A) The particle size distribution of various formulations with different feed ratios of BBR and Ce6. (B) Size distribution of BBR-Ce6 NPs at feed ratio of 1:1. Inset: The Tyndall effect exhibited by BBR-Ce6 NPssolution. (C) TEM image and size distribution of BBR-Ce6 NPs at feed

ratio of 1:1.(D) UV-vis spectra of BBR, Ce6, and BBR-Ce6 NPs. (E) Fluorescence spectra of Ce6 in DMSO and BBR-Ce6 NPs in water. (F) The UV-vis spectra of BBR-Ce6 NPs in the presence of 2 mM NaCl, DMSO, and 0.2%SDS. (G) The UV-vis spectra of BBR-Ce6 NPs in the presence of 0, 1, 5 mM Urea. (H-I) the release profiles of Ce6 and BBR from BBR-Ce6 NPs in different conditions (pH=7.4 and 5.0).

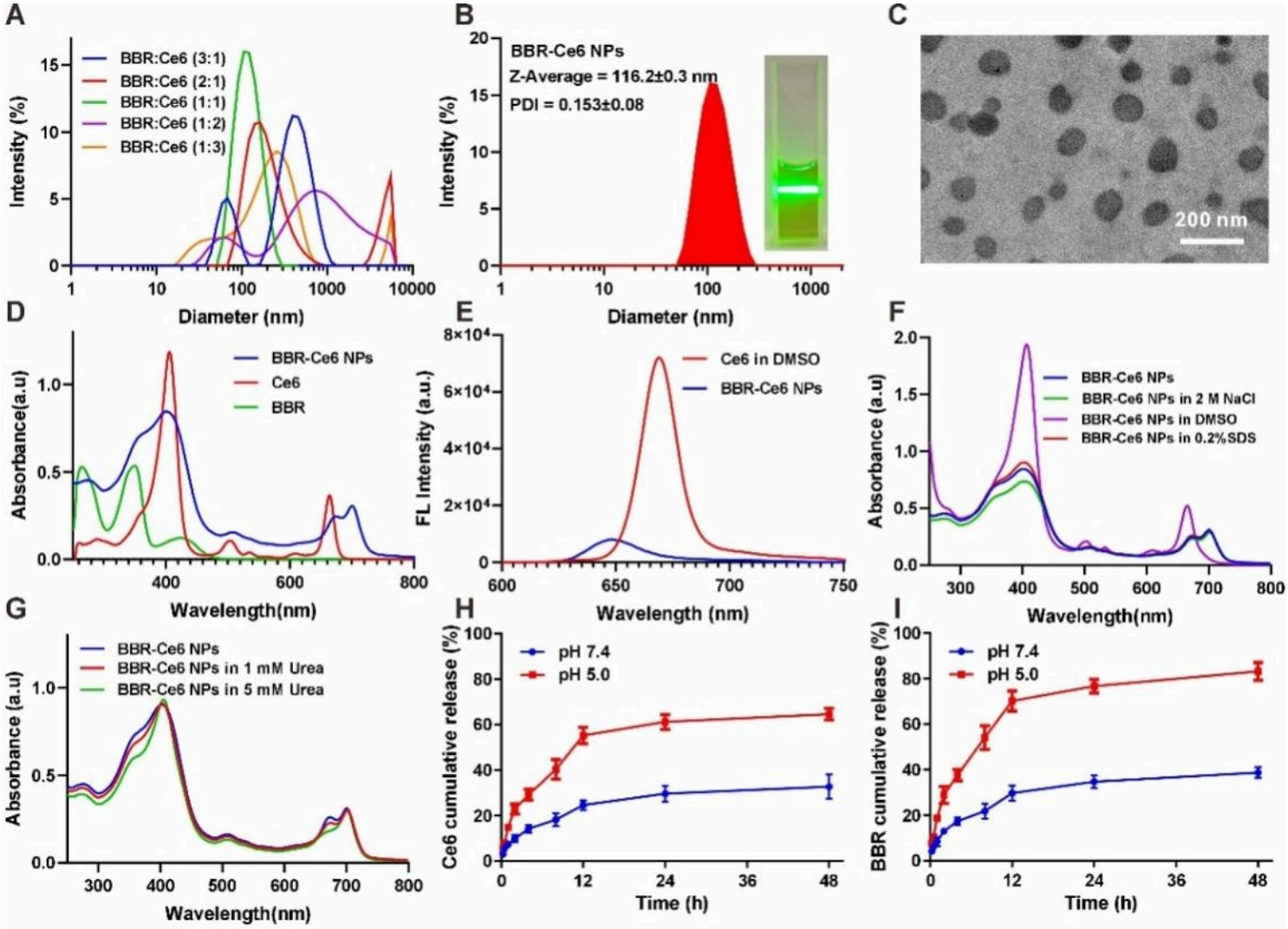


Figure 1

Characterization of BBR-Ce6 NPs(A) The particle size distribution of various formulations with different feed ratios of BBR and Ce6. (B) Size distribution of BBR-Ce6 NPs at feed ratio of 1:1. Inset: The Tyndall effect exhibited by BBR-Ce6 NPssolution. (C) TEM image and size distribution of BBR-Ce6 NPs at feed ratio of 1:1.(D) UV-vis spectra of BBR, Ce6, and BBR-Ce6 NPs. (E) Fluorescence spectra of Ce6 in DMSO and BBR-Ce6 NPs in water. (F) The UV-vis spectra of BBR-Ce6 NPs in the presence of 2 mM NaCl, DMSO, and 0.2%SDS. (G) The UV-vis spectra of BBR-Ce6 NPs in the presence of 0, 1, 5 mM Urea. (H-I) the release profiles of Ce6 and BBR from BBR-Ce6 NPs in different conditions (pH=7.4 and 5.0).

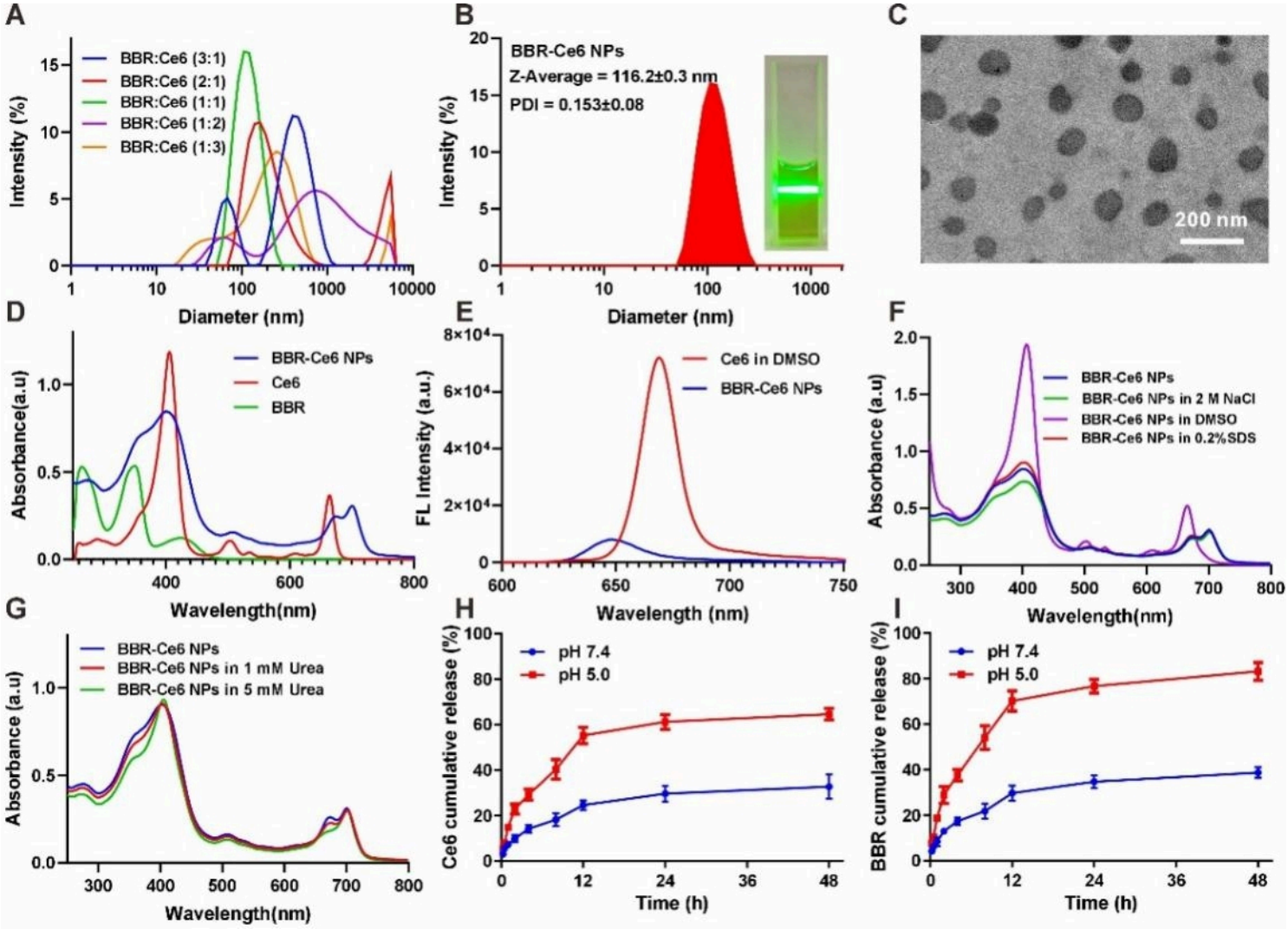


Figure 1

Characterization of BBR-Ce6 NPs(A) The particle size distribution of various formulations with different feed ratios of BBR and Ce6. (B) Size distribution of BBR-Ce6 NPs at feed ratio of 1:1. Inset: The Tyndall effect exhibited by BBR-Ce6 NPssolution. (C) TEM image and size distribution of BBR-Ce6 NPs at feed ratio of 1:1.(D) UV-vis spectra of BBR, Ce6, and BBR-Ce6 NPs. (E) Fluorescence spectra of Ce6 in DMSO and BBR-Ce6 NPs in water. (F) The UV-vis spectra of BBR-Ce6 NPs in the presence of 2 mM NaCl, DMSO, and 0.2%SDS. (G) The UV-vis spectra of BBR-Ce6 NPs in the presence of 0, 1, 5 mM Urea. (H-I) the release profiles of Ce6 and BBR from BBR-Ce6 NPs in different conditions (pH=7.4 and 5.0).

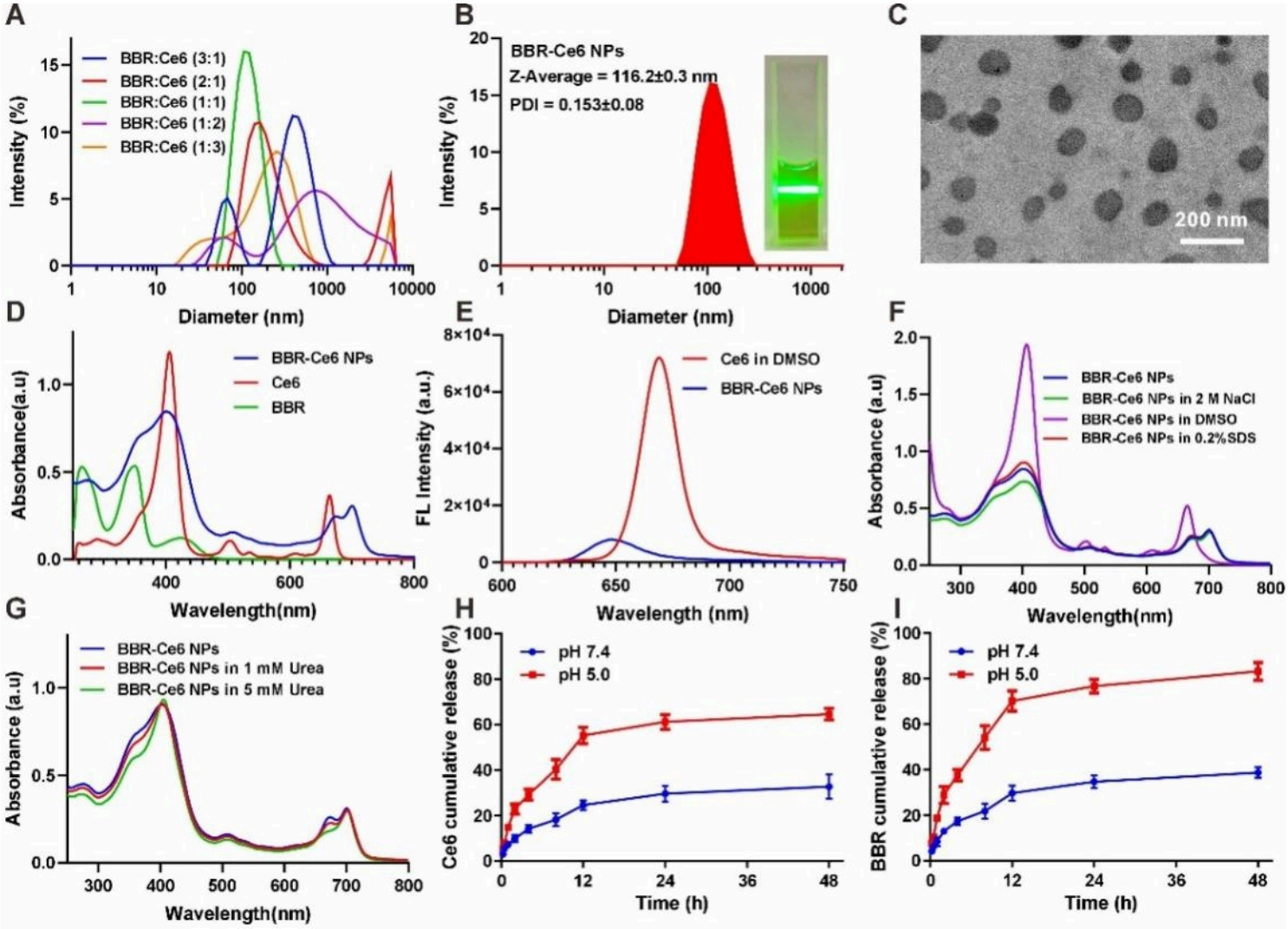


Figure 1

Characterization of BBR-Ce6 NPs(A) The particle size distribution of various formulations with different feed ratios of BBR and Ce6. (B) Size distribution of BBR-Ce6 NPs at feed ratio of 1:1. Inset: The Tyndall effect exhibited by BBR-Ce6 NPssolution. (C) TEM image and size distribution of BBR-Ce6 NPs at feed ratio of 1:1.(D) UV-vis spectra of BBR, Ce6, and BBR-Ce6 NPs. (E) Fluorescence spectra of Ce6 in DMSO and BBR-Ce6 NPs in water. (F) The UV-vis spectra of BBR-Ce6 NPs in the presence of 2 mM NaCl, DMSO, and 0.2%SDS. (G) The UV-vis spectra of BBR-Ce6 NPs in the presence of 0, 1, 5 mM Urea. (H-I) the release profiles of Ce6 and BBR from BBR-Ce6 NPs in different conditions (pH=7.4 and 5.0).

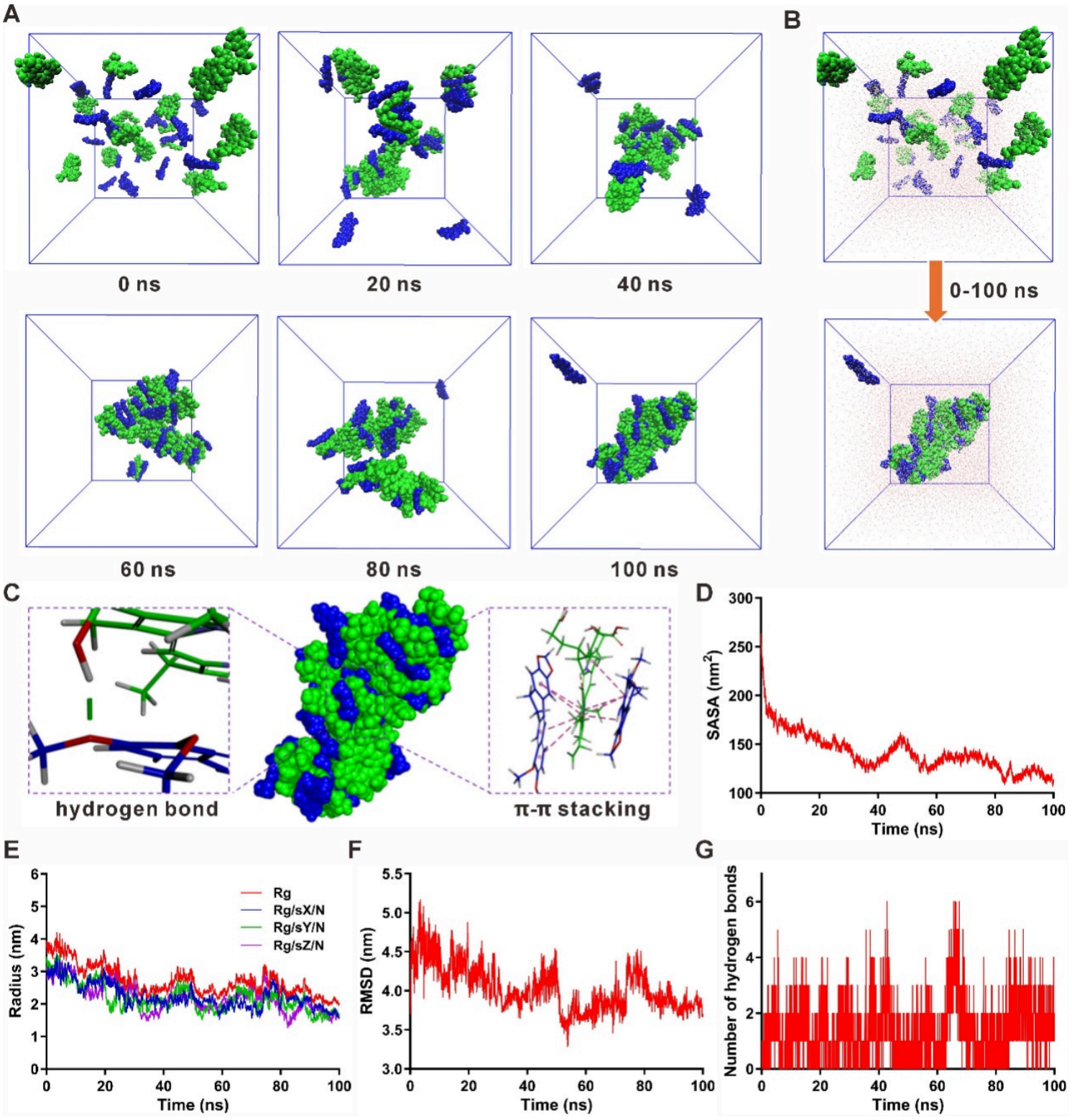


Figure 2

Molecular dynamic simulation of BBR-Ce6 NPs. (A) Snapshot pictures of self-assembly BBR (blue)/Ce6 (green) system over a 100 ns time scale. (B) The structural changes of A and B, as well as water, in the initial and end states under molecular simulation conditions. (C) Molecular interaction of the BBR-Ce6 system. (D-F) Solvent-accessible surface area (SASA), radius of gyration (Rg) and variation in root-mean-

square deviation (RMSD) of BBR-Ce6 NPs as a function of time. (G) The change in the number of intermolecular hydrogen bonds during the 100-ns self-assembly of BBR and Ce6.

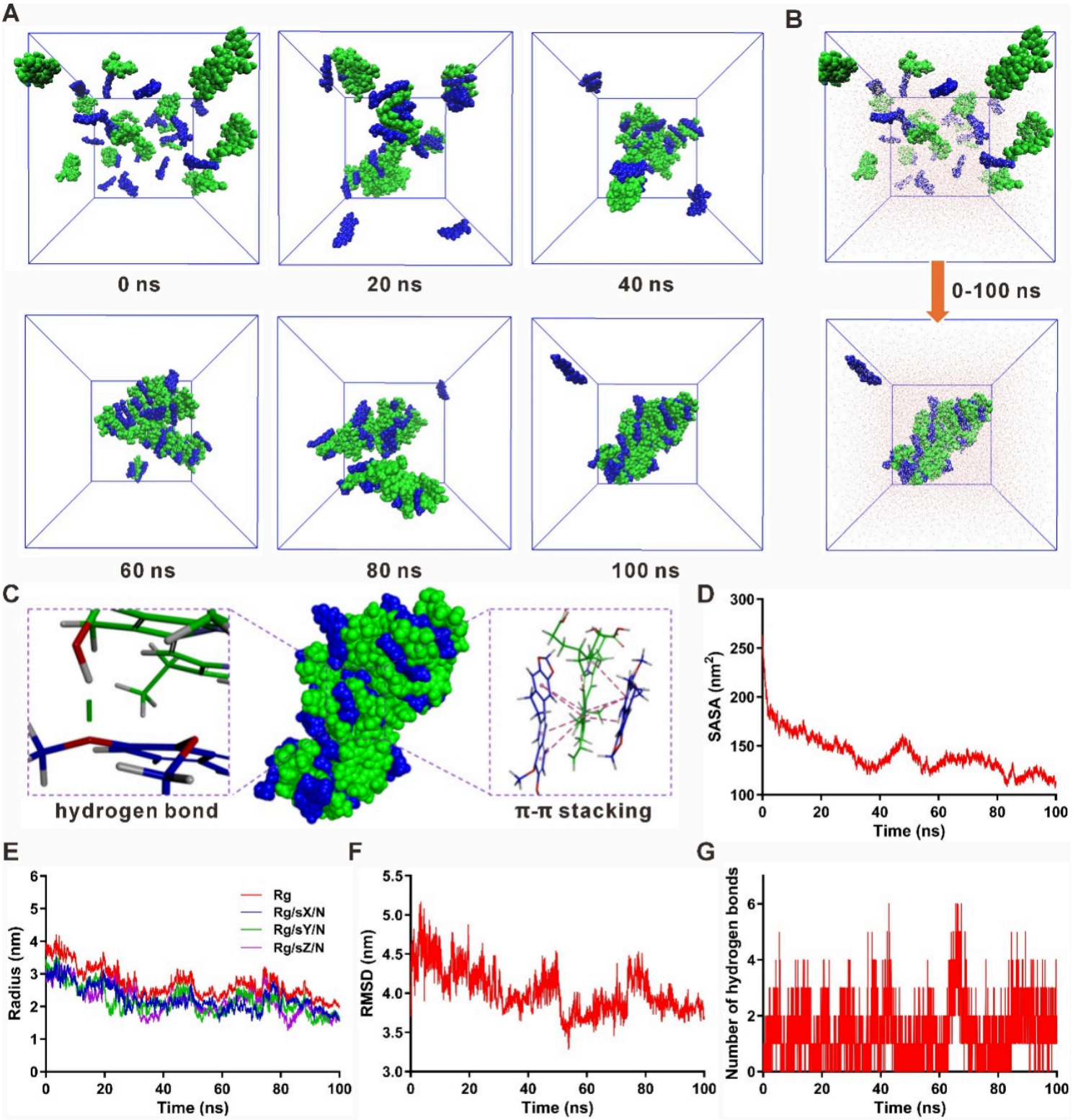


Figure 2

Molecular dynamic simulation of BBR-Ce6 NPs. (A) Snapshot pictures of self-assembly BBR (blue)/Ce6 (green) system over a 100 ns time scale. (B) The structural changes of A and B, as well as water, in the

initial and end states under molecular simulation conditions. (C) Molecular interaction of the BBR-Ce6 system. (D-F) Solvent-accessible surface area (SASA), radius of gyration (Rg) and variation in root-mean-square deviation (RMSD) of BBR-Ce6 NPs as a function of time. (G) The change in the number of intermolecular hydrogen bonds during the 100-ns self-assembly of BBR and Ce6.

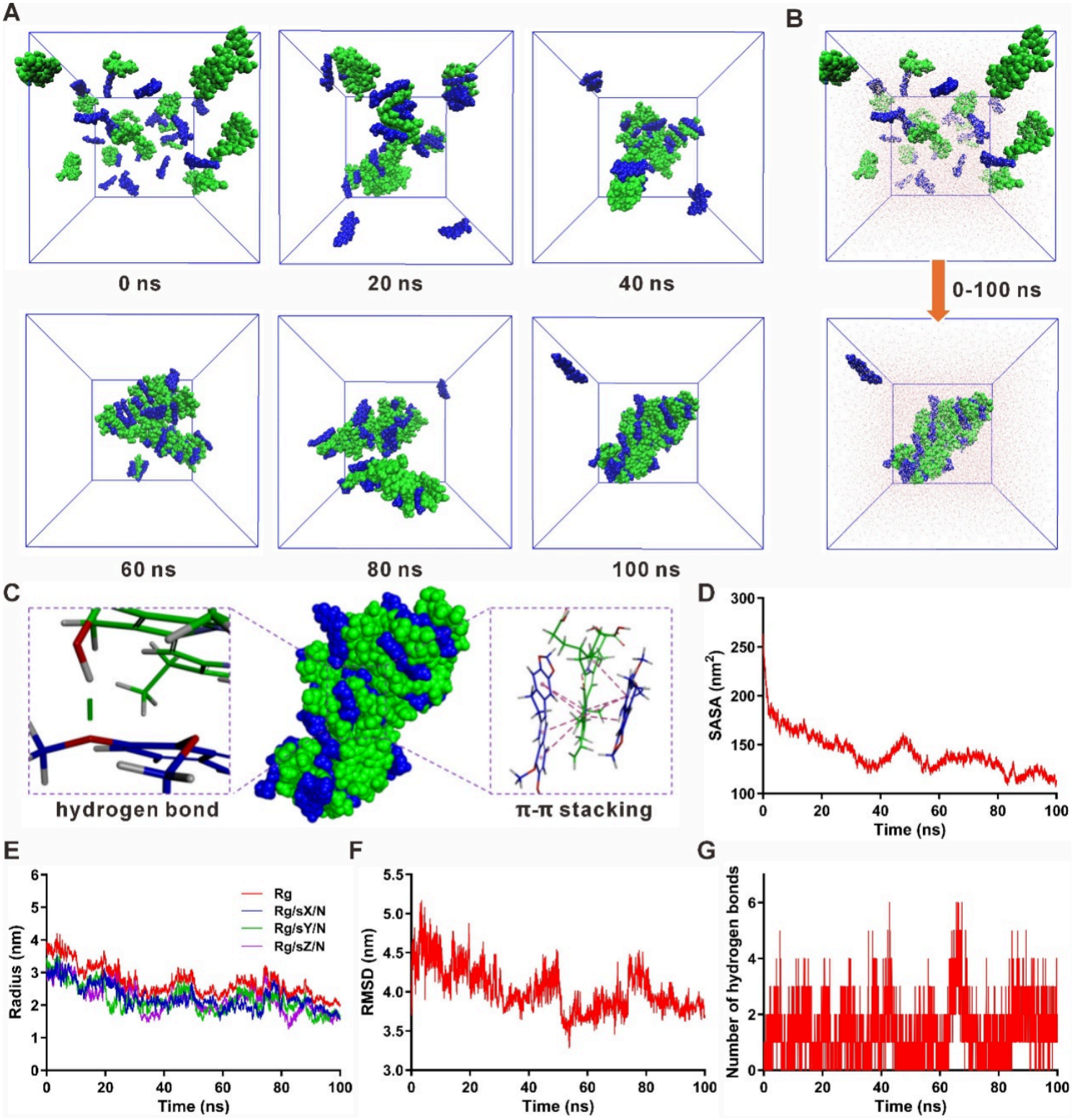


Figure 2

Molecular dynamic simulation of BBR-Ce6 NPs. (A) Snapshot pictures of self-assembly BBR (blue)/Ce6 (green) system over a 100 ns time scale. (B) The structural changes of A and B, as well as water, in the initial and end states under molecular simulation conditions. (C) Molecular interaction of the BBR-Ce6 system. (D-F) Solvent-accessible surface area (SASA), radius of gyration (Rg) and variation in root-mean-square deviation (RMSD) of BBR-Ce6 NPs as a function of time. (G) The change in the number of intermolecular hydrogen bonds during the 100-ns self-assembly of BBR and Ce6.

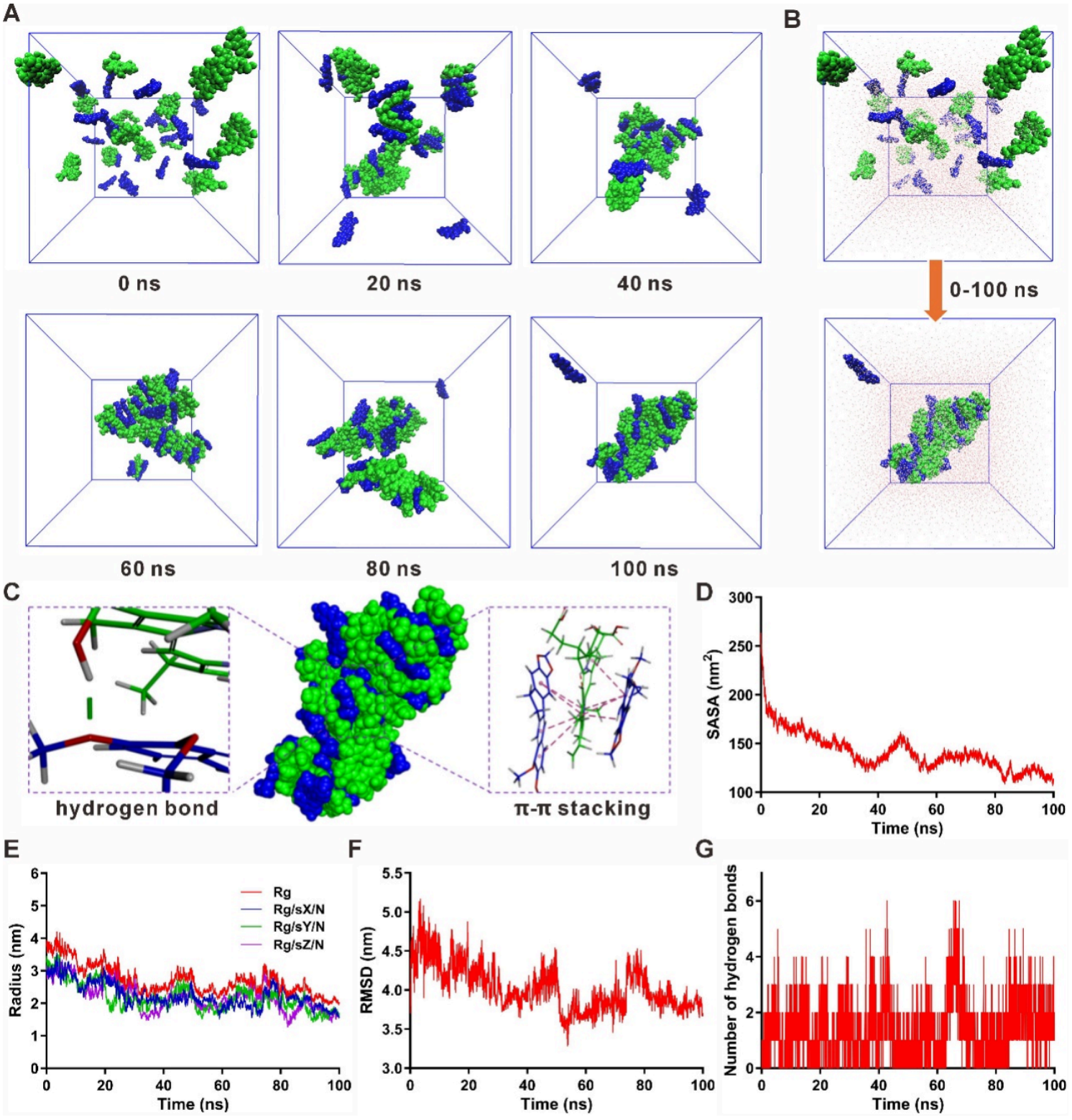


Figure 2

Molecular dynamic simulation of BBR-Ce6 NPs. (A) Snapshot pictures of self-assembly BBR (blue)/Ce6 (green) system over a 100 ns time scale. (B) The structural changes of A and B, as well as water, in the initial and end states under molecular simulation conditions. (C) Molecular interaction of the BBR-Ce6 system. (D-F) Solvent-accessible surface area (SASA), radius of gyration (Rg) and variation in root-mean-square deviation (RMSD) of BBR-Ce6 NPs as a function of time. (G) The change in the number of intermolecular hydrogen bonds during the 100-ns self-assembly of BBR and Ce6.

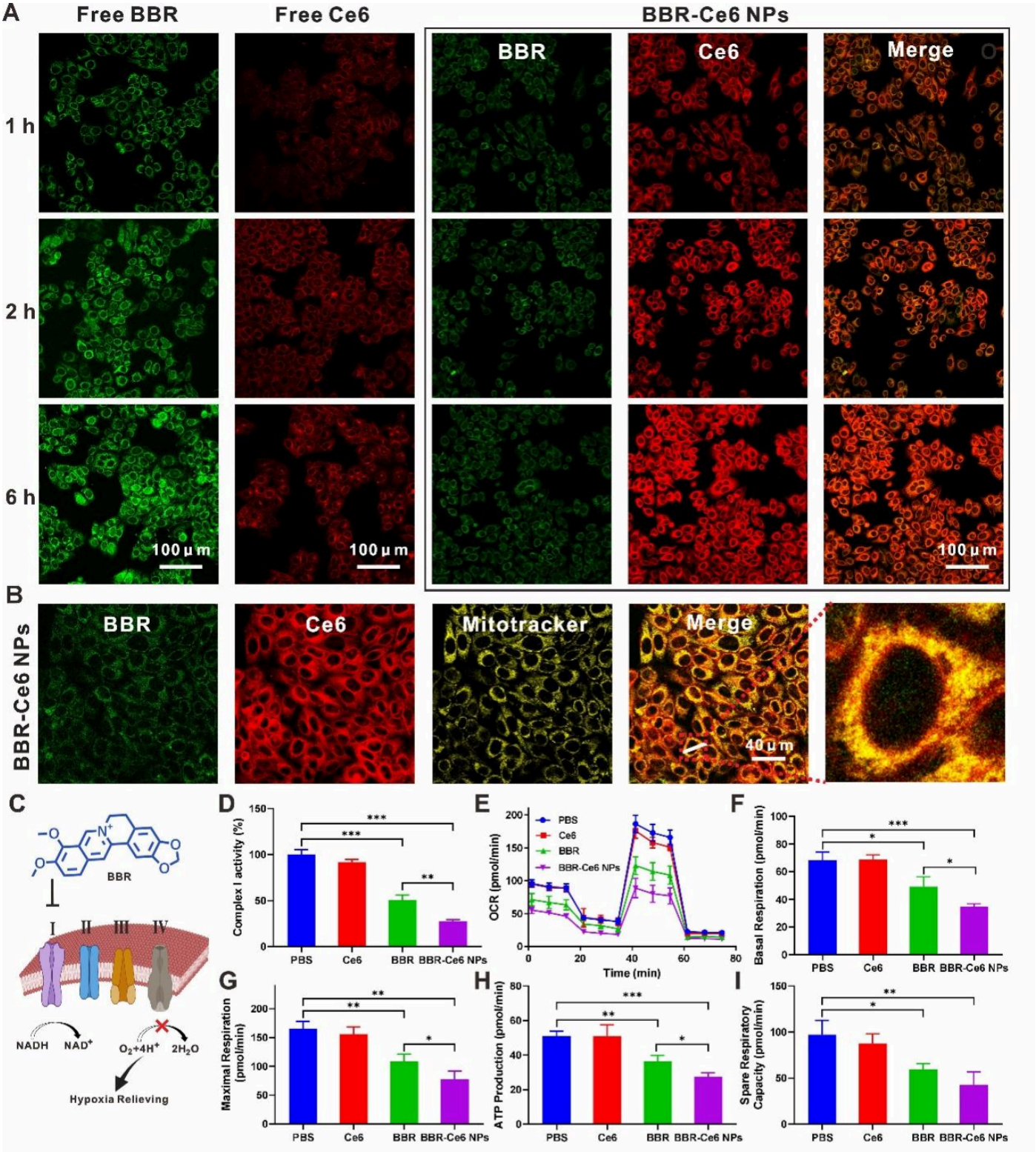


Figure 3

Enhanced cellular uptake, mitochondrial targeting, and hypoxia alleviation capability of BBR-Ce6 NPs. (A) CLSM images of HepG2 cells after treatment with free BBR, free Ce6, and BBR-Ce6 NPs for 1, 2, or 6 h. (B) Colocalized with Mitotracker after 6 h of BBR-Ce6 NPs treatment. (C) Schematic diagram of the BBR-mediated hypoxia alleviation mechanism. (D) Relative complex I activity of HepG2 cells after treatment with PBS, Ce6, BBR, or BBR-Ce6 NPs. (E) OCR analysis of HepG2 cells after treatment with PBS, Ce6,

BBR, or BBR-Ce6 NPs. (F-I) The basal respiration, maximal respiration, ATP production, and spare respiratory capacity of HepG2 cells pretreated with PBS, Ce6, BBR, or BBR-Ce6 NPs.

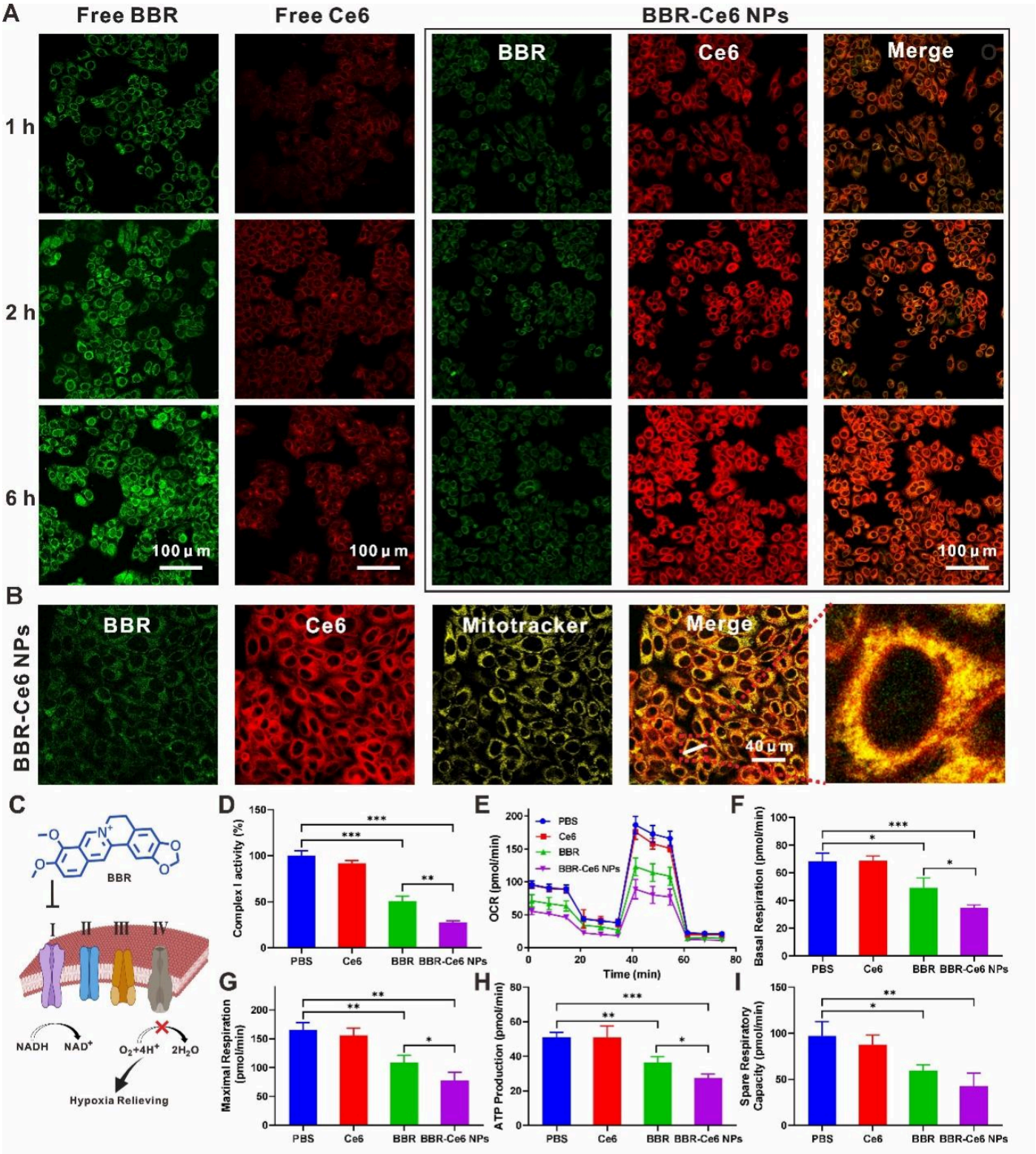


Figure 3

Enhanced cellular uptake, mitochondrial targeting, and hypoxia alleviation capability of BBR-Ce6 NPs. (A) CLSM images of HepG2 cells after treatment with free BBR, free Ce6, and BBR-Ce6 NPs for 1, 2, or 6 h.

(B) Colocalized with Mitotracker after 6 h of BBR-Ce6 NPs treatment. (C) Schematic diagram of the BBR-mediated hypoxia alleviation mechanism. (D) Relative complex I activity of HepG2 cells after treatment with PBS, Ce6, BBR, or BBR-Ce6 NPs. (E) OCR analysis of HepG2 cells after treatment with PBS, Ce6, BBR, or BBR-Ce6 NPs. (F-I) The basal respiration, maximal respiration, ATP production, and spare respiratory capacity of HepG2 cells pretreated with PBS, Ce6, BBR, or BBR-Ce6 NPs.

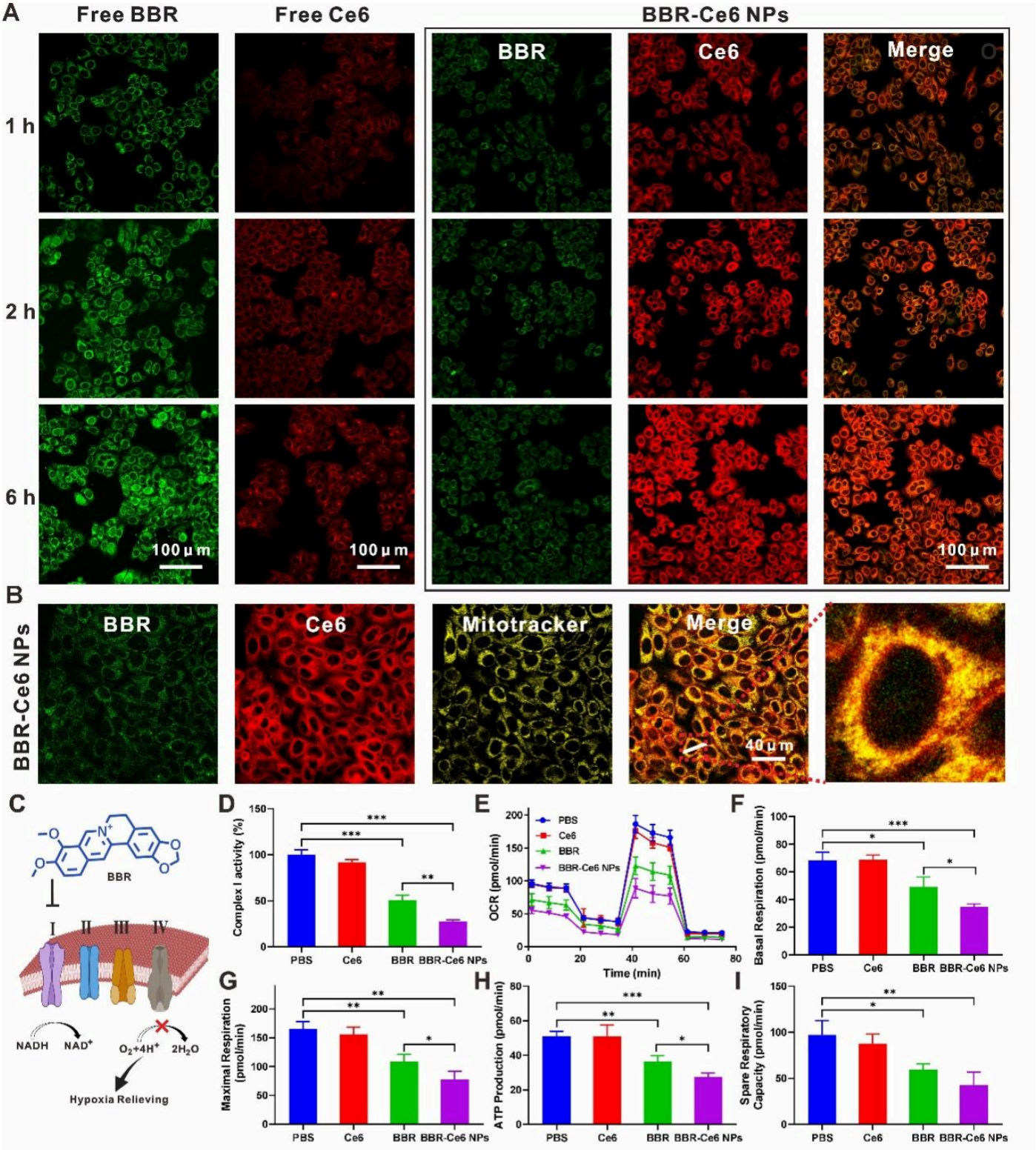


Figure 3

Enhanced cellular uptake, mitochondrial targeting, and hypoxia alleviation capability of BBR-Ce6 NPs. (A) CLSM images of HepG2 cells after treatment with free BBR, free Ce6, and BBR-Ce6 NPs for 1, 2, or 6 h. (B) Colocalized with Mitotracker after 6 h of BBR-Ce6 NPs treatment. (C) Schematic diagram of the BBR-mediated hypoxia alleviation mechanism. (D) Relative complex I activity of HepG2 cells after treatment with PBS, Ce6, BBR, or BBR-Ce6 NPs. (E) OCR analysis of HepG2 cells after treatment with PBS, Ce6, BBR, or BBR-Ce6 NPs. (F-I) The basal respiration, maximal respiration, ATP production, and spare respiratory capacity of HepG2 cells pretreated with PBS, Ce6, BBR, or BBR-Ce6 NPs.

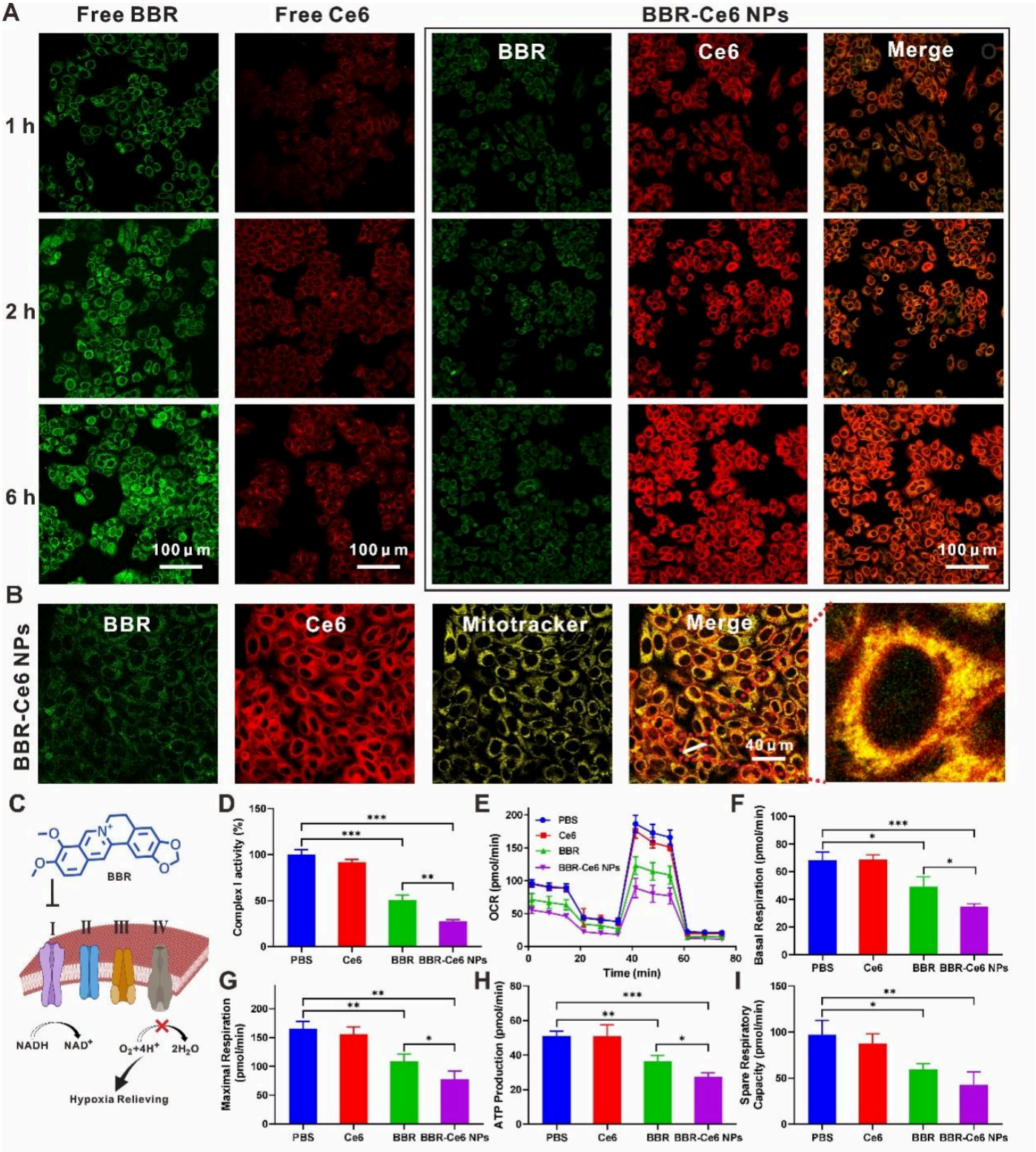


Figure 3

Enhanced cellular uptake, mitochondrial targeting, and hypoxia alleviation capability of BBR-Ce6 NPs. (A) CLSM images of HepG2 cells after treatment with free BBR, free Ce6, and BBR-Ce6 NPs for 1, 2, or 6 h. (B) Colocalized with Mitotracker after 6 h of BBR-Ce6 NPs treatment. (C) Schematic diagram of the BBR-mediated hypoxia alleviation mechanism. (D) Relative complex I activity of HepG2 cells after treatment with PBS, Ce6, BBR, or BBR-Ce6 NPs. (E) OCR analysis of HepG2 cells after treatment with PBS, Ce6, BBR, or BBR-Ce6 NPs. (F-I) The basal respiration, maximal respiration, ATP production, and spare respiratory capacity of HepG2 cells pretreated with PBS, Ce6, BBR, or BBR-Ce6 NPs.

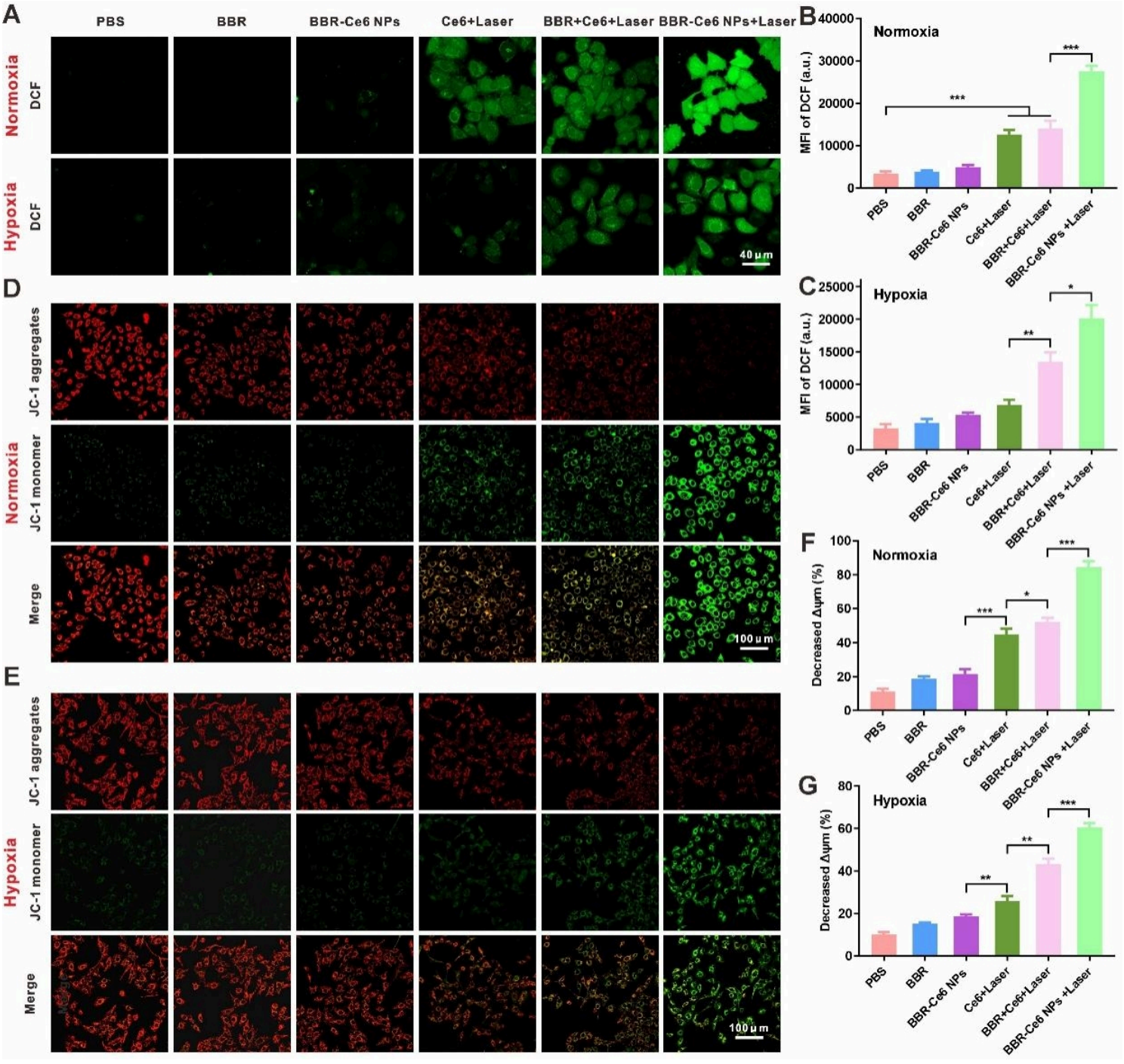


Figure 4

Changes in BBR-Ce6 NPs-mediated reactive oxygen species generation capacity and mitochondrial membrane potential under normoxic and hypoxic conditions. (A) CLSM images of ROS levels in HepG2 cells with different treatments under normoxic and hypoxic conditions. (B-C) Quantitative analysis of the intracellular ROS level by flow cytometry under normoxic and hypoxic conditions. (D-E) The CLSM results of mitochondrial membrane potential of HepG2 cells treated with various formulations under normoxic and hypoxic conditions. (F-G) Quantitative ratio of decreased mitochondrial membrane potential under normoxic and hypoxic conditions.

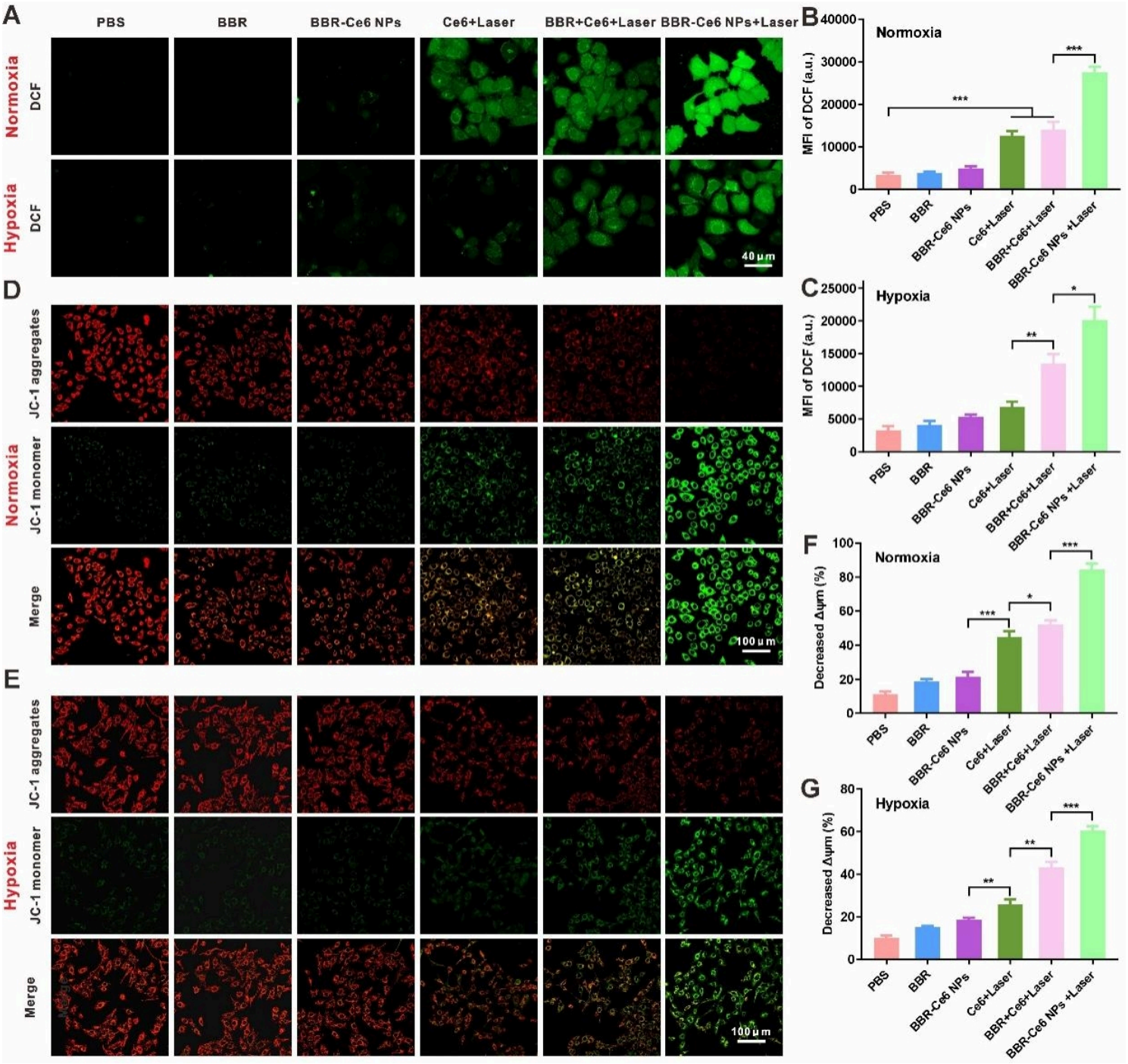


Figure 4

Changes in BBR-Ce6 NPs-mediated reactive oxygen species generation capacity and mitochondrial membrane potential under normoxic and hypoxic conditions. (A) CLSM images of ROS levels in HepG2 cells with different treatments under normoxic and hypoxic conditions. (B-C) Quantitative analysis of the intracellular ROS level by flow cytometry under normoxic and hypoxic conditions. (D-E) The CLSM results of mitochondrial membrane potential of HepG2 cells treated with various formulations under normoxic and hypoxic conditions. (F-G) Quantitative ratio of decreased mitochondrial membrane potential under normoxic and hypoxic conditions.

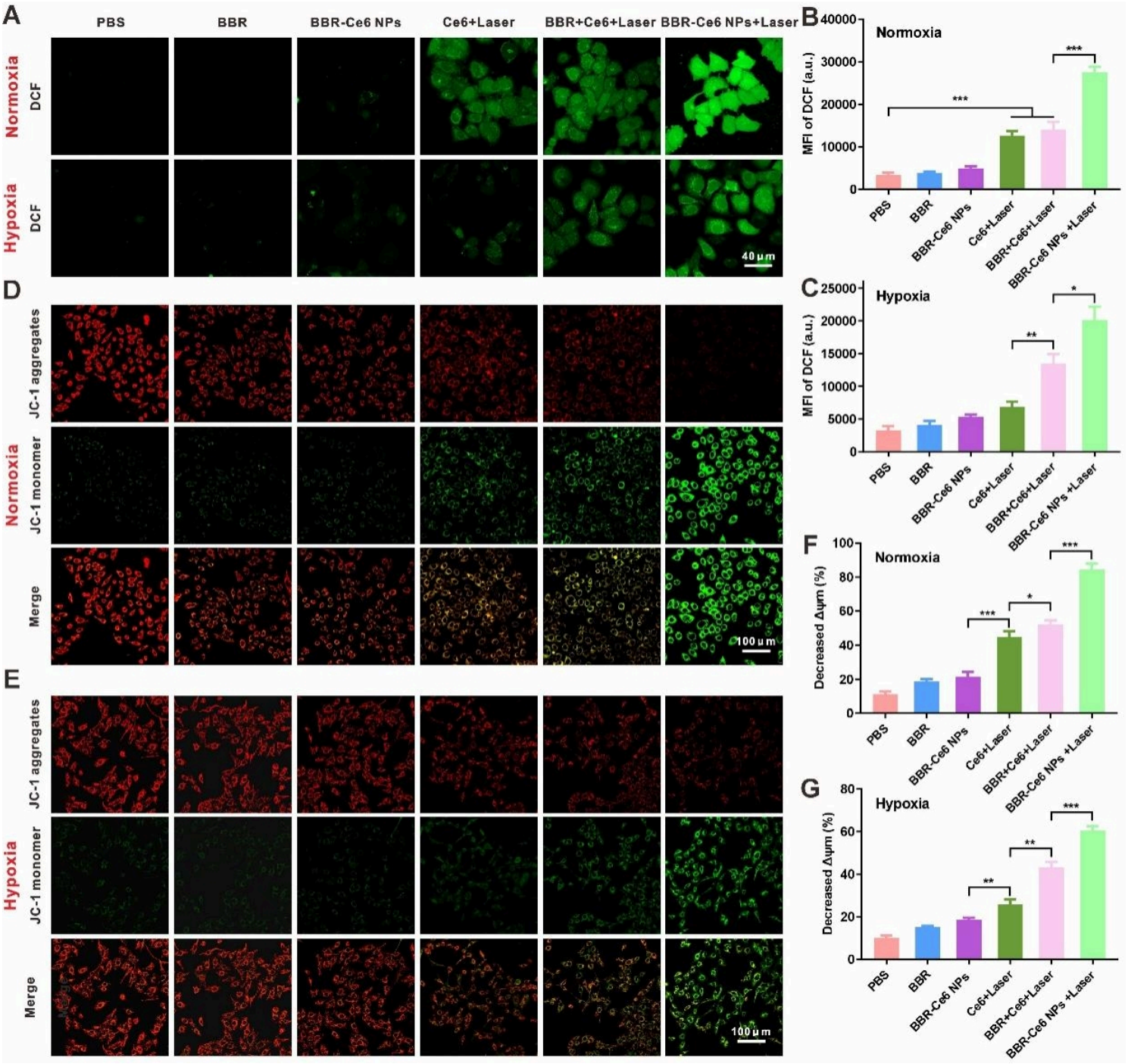


Figure 4

Changes in BBR-Ce6 NPs-mediated reactive oxygen species generation capacity and mitochondrial membrane potential under normoxic and hypoxic conditions. (A) CLSM images of ROS levels in HepG2 cells with different treatments under normoxic and hypoxic conditions. (B-C) Quantitative analysis of the intracellular ROS level by flow cytometry under normoxic and hypoxic conditions. (D-E) The CLSM results of mitochondrial membrane potential of HepG2 cells treated with various formulations under normoxic and hypoxic conditions. (F-G) Quantitative ratio of decreased mitochondrial membrane potential under normoxic and hypoxic conditions.

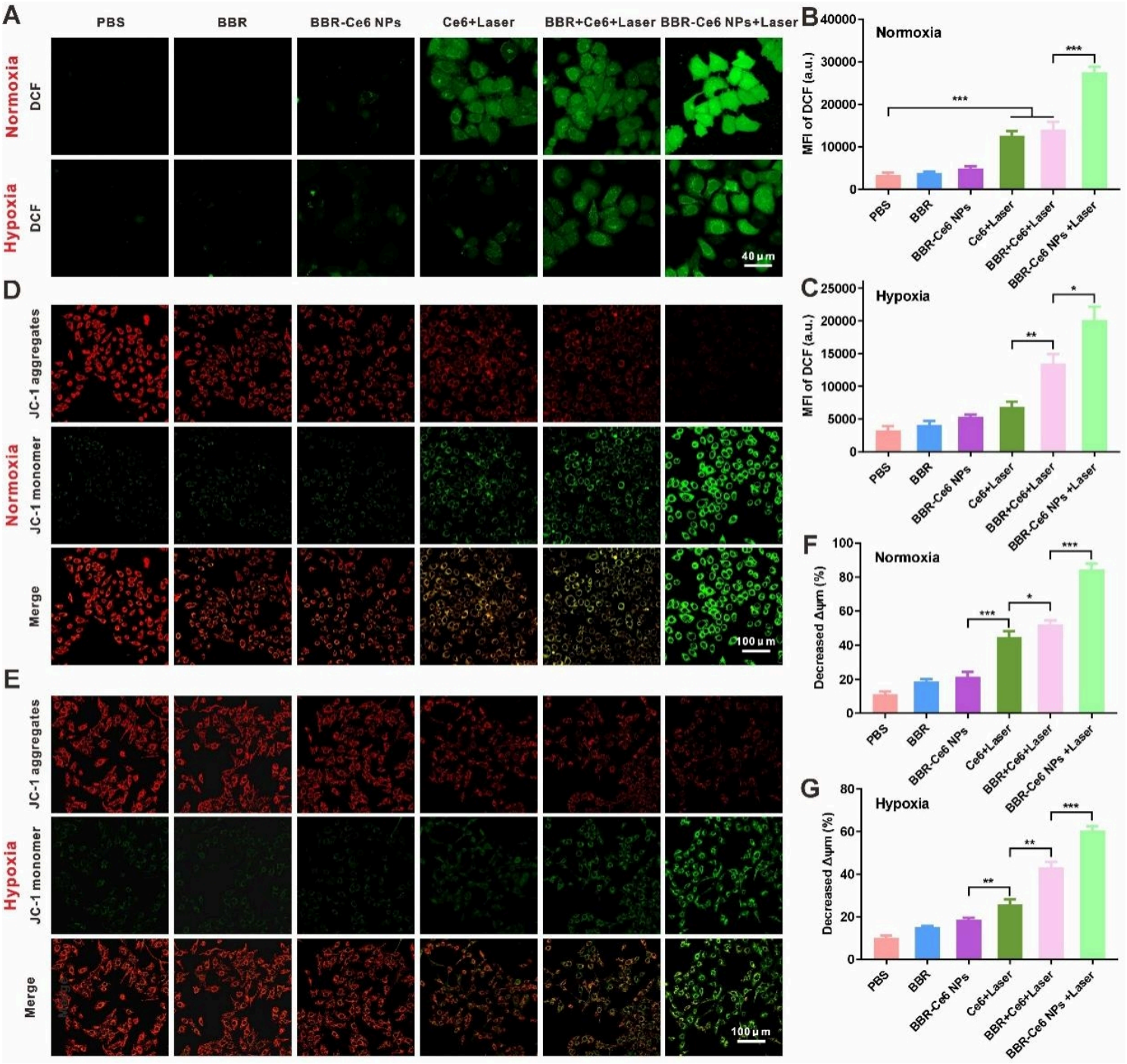


Figure 4

Changes in BBR-Ce6 NPs-mediated reactive oxygen species generation capacity and mitochondrial membrane potential under normoxic and hypoxic conditions. (A) CLSM images of ROS levels in HepG2 cells with different treatments under normoxic and hypoxic conditions. (B-C) Quantitative analysis of the intracellular ROS level by flow cytometry under normoxic and hypoxic conditions. (D-E) The CLSM results of mitochondrial membrane potential of HepG2 cells treated with various formulations under normoxic and hypoxic conditions. (F-G) Quantitative ratio of decreased mitochondrial membrane potential under normoxic and hypoxic conditions.

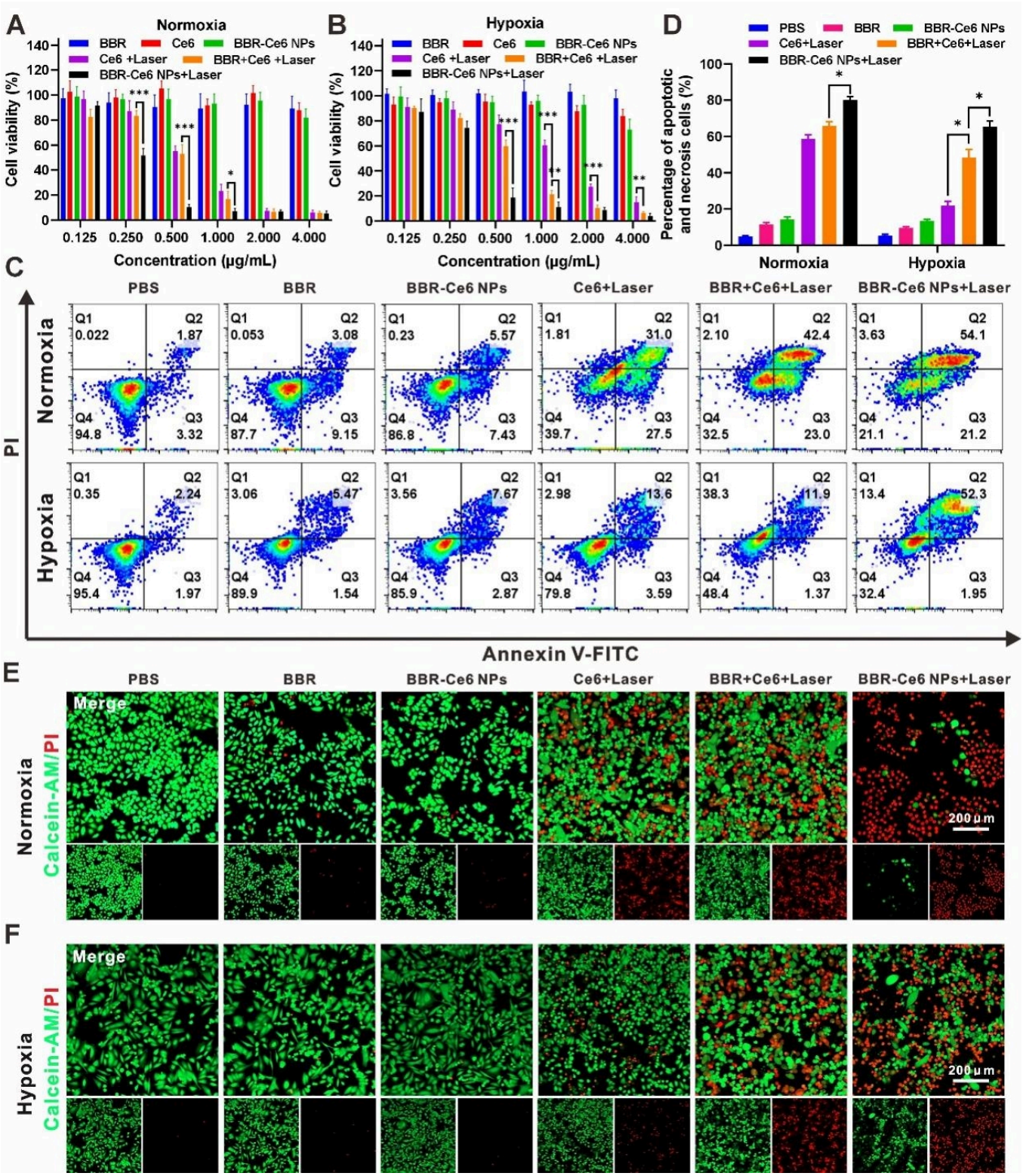


Figure 5

In vitro PDT effect of BBR-Ce6 NPs under normoxia or hypoxia condition. (A-B) Cell viability of HepG2 cells after incubation with various formulations normoxic and hypoxic conditions. (C) Apoptosis analysis by flow cytometry of HepG2 cells after treatment with various formulations under normoxia or hypoxia condition. (D) Quantitative analysis of different cell populations after incubation with various formulations under normoxic and hypoxic conditions. (E-F) Live/dead cell staining of HepG2 cells after treatment with various formulations under normoxia or hypoxia condition.

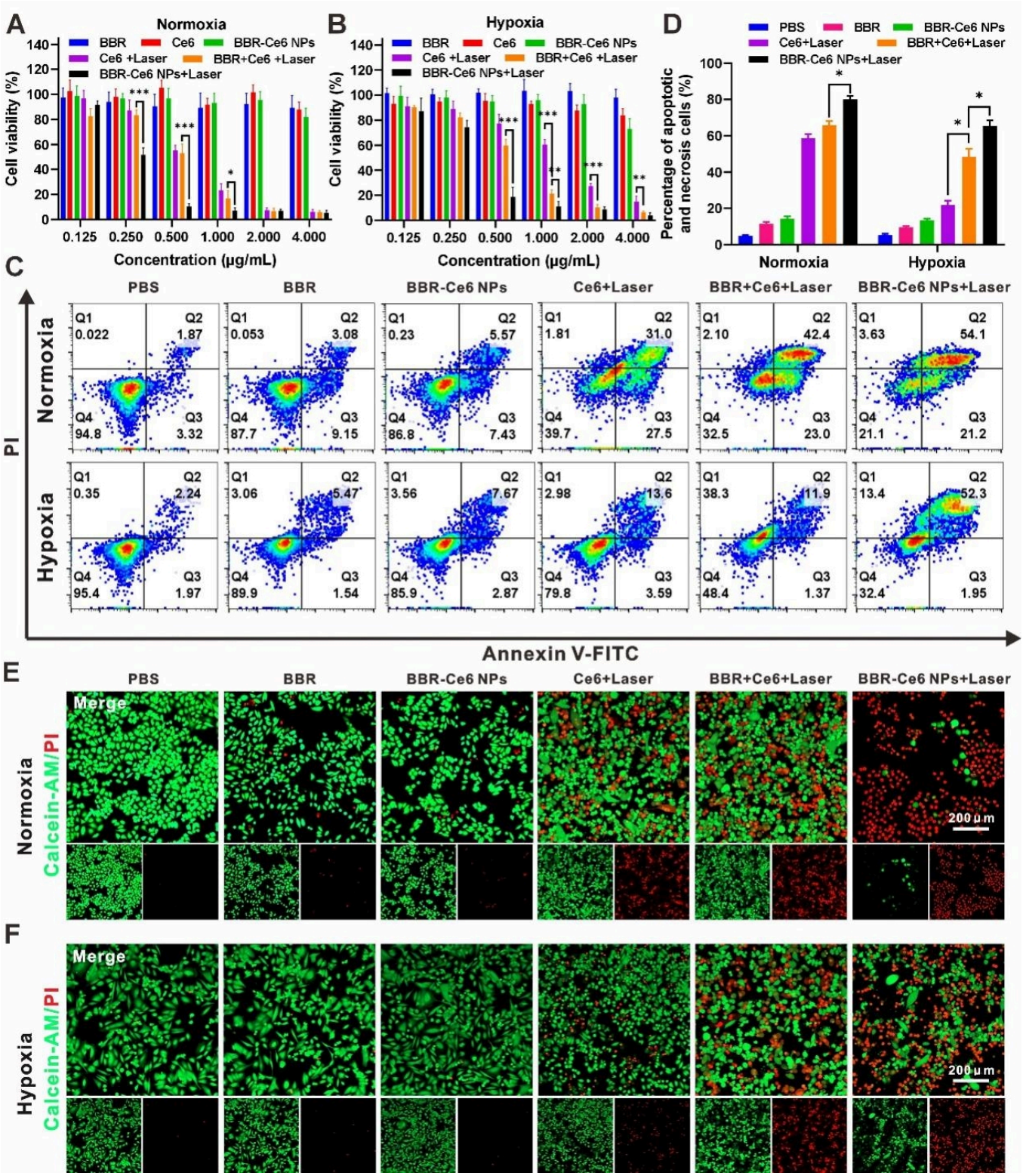


Figure 5

In vitro PDT effect of BBR-Ce6 NPs under normoxia or hypoxia condition. (A-B) Cell viability of HepG2 cells after incubation with various formulations normoxic and hypoxic conditions. (C) Apoptosis analysis by flow cytometry of HepG2 cells after treatment with various formulations under normoxia or hypoxia condition. (D) Quantitative analysis of different cell populations after incubation with various

formulations under normoxic and hypoxic conditions. (E-F) Live/dead cell staining of HepG2 cells after treatment with various formulations under normoxia or hypoxia condition.

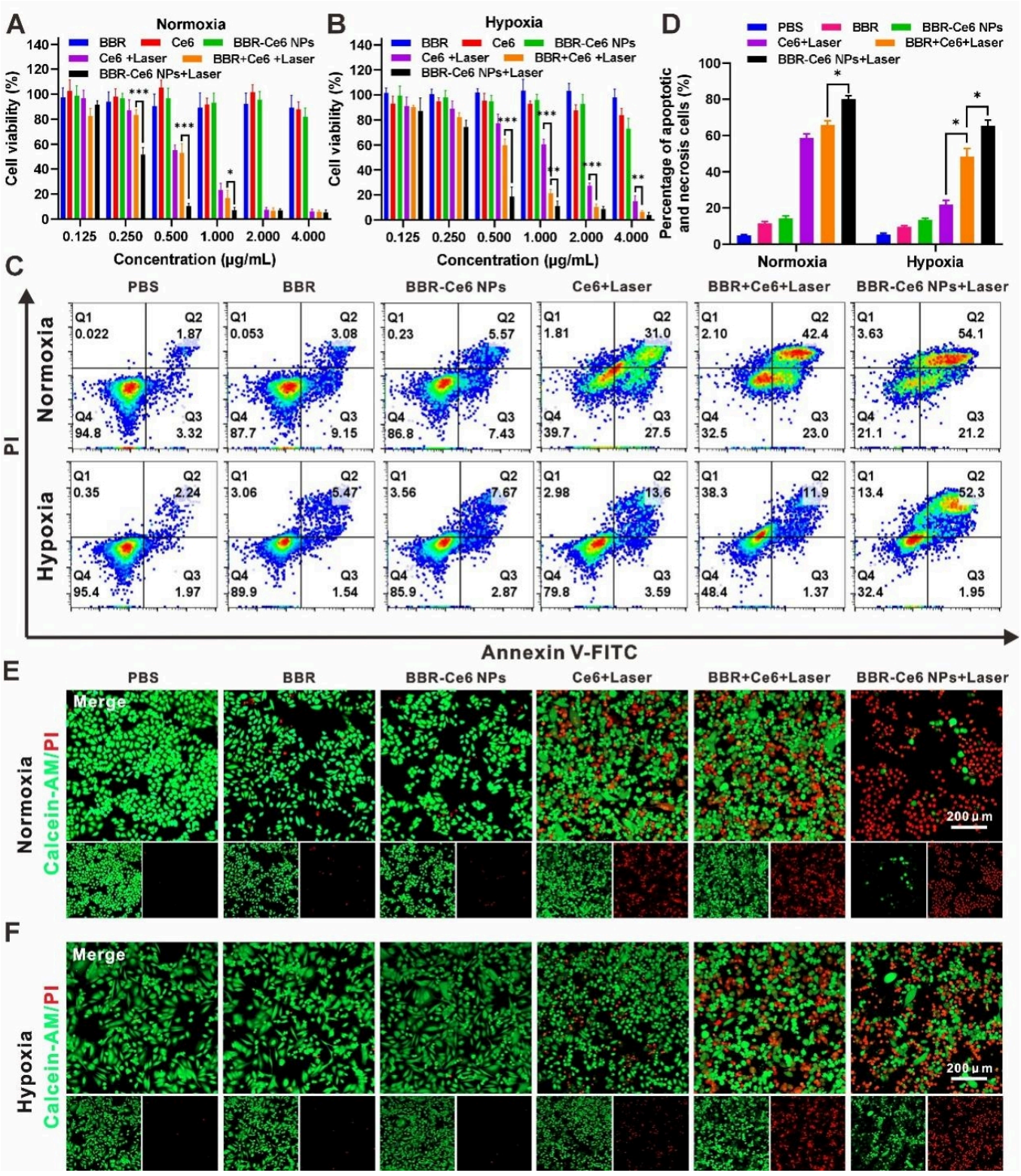


Figure 5

In vitro PDT effect of BBR-Ce6 NPs under normoxia or hypoxia condition. (A-B) Cell viability of HepG2 cells after incubation with various formulations normoxic and hypoxic conditions. (C) Apoptosis analysis

by flow cytometry of HepG2 cells after treatment with various formulations under normoxia or hypoxia condition. (D) Quantitative analysis of different cell populations after incubation with various formulations under normoxic and hypoxic conditions. (E-F) Live/dead cell staining of HepG2 cells after treatment with various formulations under normoxia or hypoxia condition.

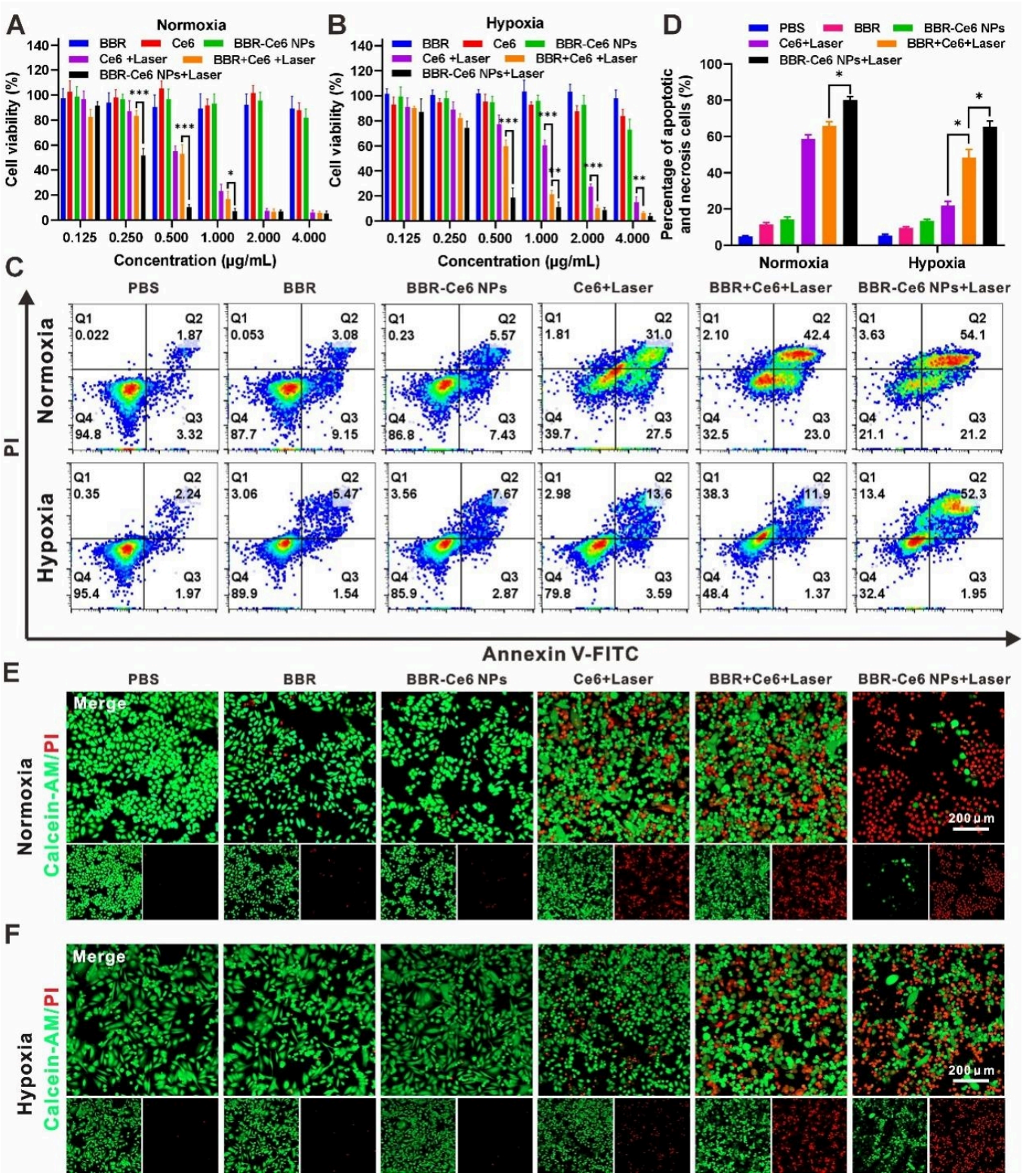


Figure 5

In vitro PDT effect of BBR-Ce6 NPs under normoxia or hypoxia condition. (A-B) Cell viability of HepG2 cells after incubation with various formulations normoxic and hypoxic conditions. (C) Apoptosis analysis by flow cytometry of HepG2 cells after treatment with various formulations under normoxia or hypoxia condition. (D) Quantitative analysis of different cell populations after incubation with various formulations under normoxic and hypoxic conditions. (E-F) Live/dead cell staining of HepG2 cells after treatment with various formulations under normoxia or hypoxia condition.

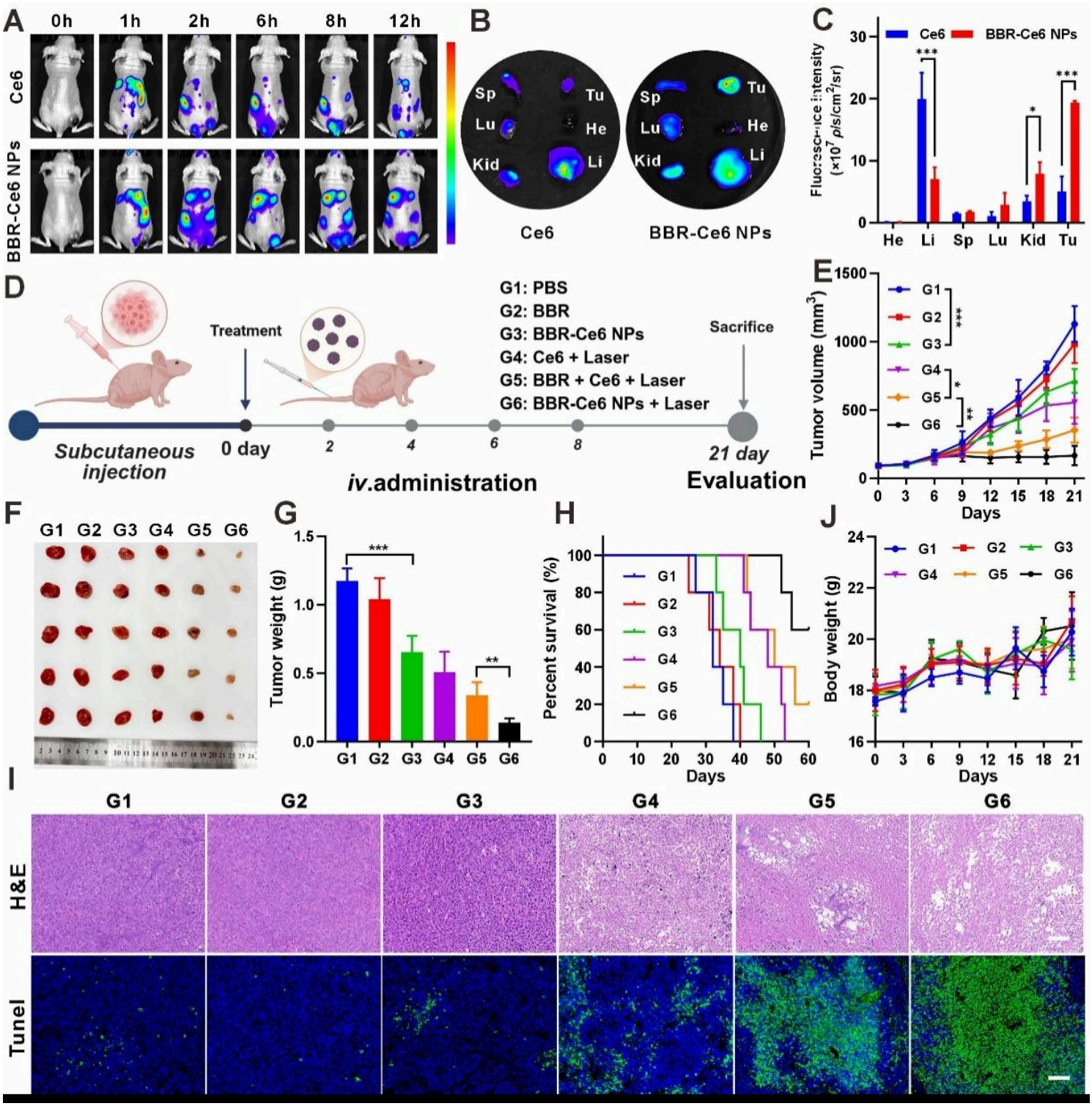


Figure 6

Antitumor studies of BBR-Ce6 NPs *in vivo*. (A) *In vivo* fluorescence images of HepG2 tumor-bearing mice at different time points (0, 1, 2, 6, 8, and 12 h) after intravenous injection of Ce6 or BBR-Ce6 NPs. (B) Ex vivo fluorescence images of organs and tumors after 12 h post administration. (C) Semi-quantitative analysis of the fluorescence intensity of excised tissues and tumors in (B). (D) Diagram of the establishment of tumor-bearing mice and the entire treatment process. (E) Progression of tumor volume in mice under different treatment groups. (F) Photographs of tumor tissues dissected from each treatment group on day 21. (G) The average weight of the tumors dissected from each group after treatment. (H) Body weight changes of HepG2 tumor-bearing mice in G1-G6 groups during the treatment period. (I) Survival curves of mice after different treatments. (J) H&E and TUNEL staining analysis of tumor tissues after various treatments. Scale bar: 100 μm.

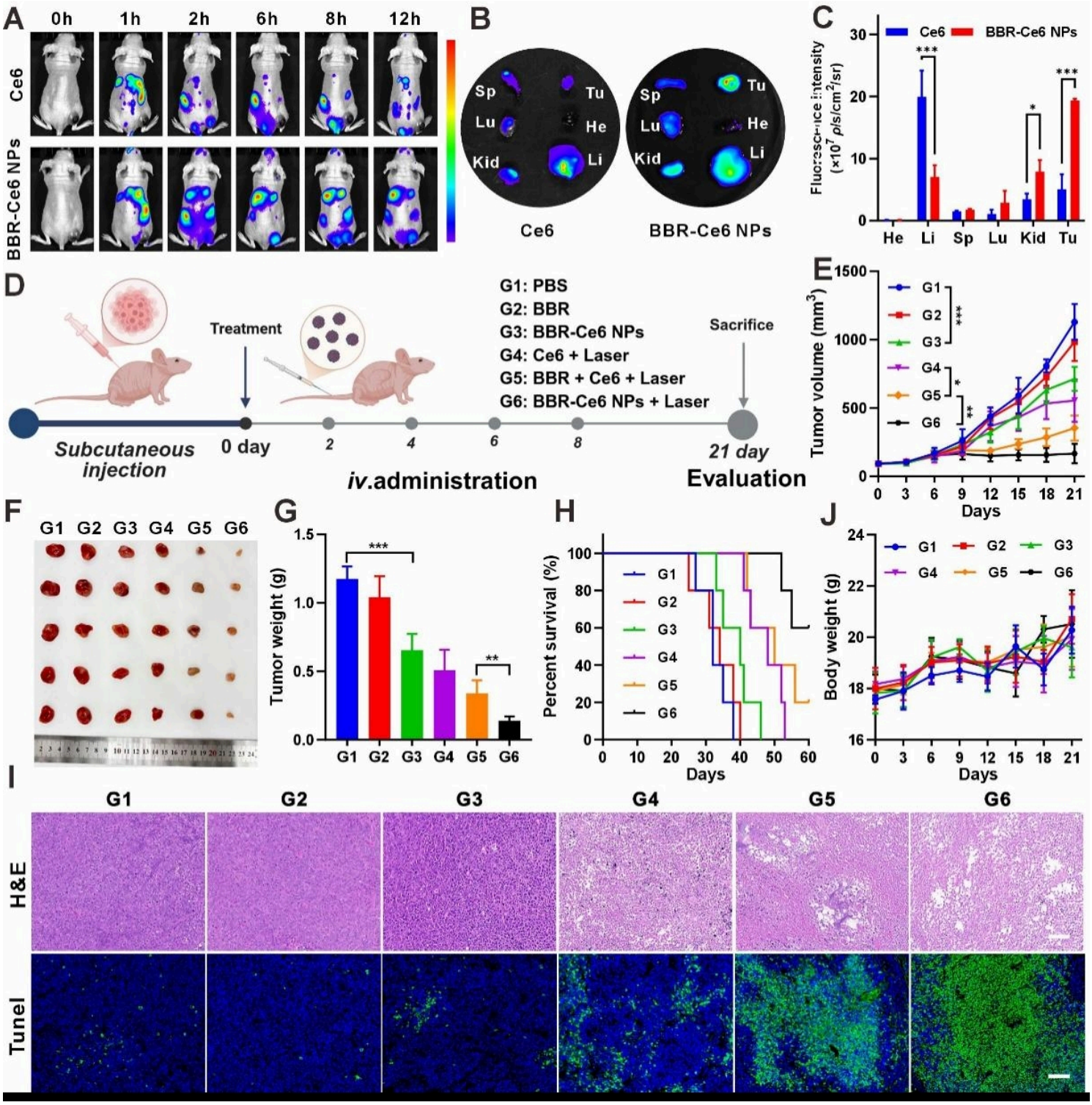


Figure 6

Antitumor studies of BBR-Ce6 NPs *in vivo*. (A) *In vivo* fluorescence images of HepG2 tumor-bearing mice at different time points (0, 1, 2, 6, 8, and 12 h) after intravenous injection of Ce6 or BBR-Ce6 NPs. (B) Ex vivo fluorescence images of organs and tumors after 12 h post administration. (C) Semi-quantitative analysis of the fluorescence intensity of excised tissues and tumors in (B). (D) Diagram of the establishment of tumor-bearing mice and the entire treatment process. (E) Progression of tumor volume in mice under different treatment groups. (F) Photographs of tumor tissues dissected from each

treatment group on day 21. (G) The average weight of the tumors dissected from each group after treatment. (H) Body weight changes of HepG2 tumor-bearing mice in G1-G6 groups during the treatment period. (I) Survival curves of mice after different treatments. (J) H&E and TUNEL staining analysis of tumor tissues after various treatments. Scale bar: 100 μm.

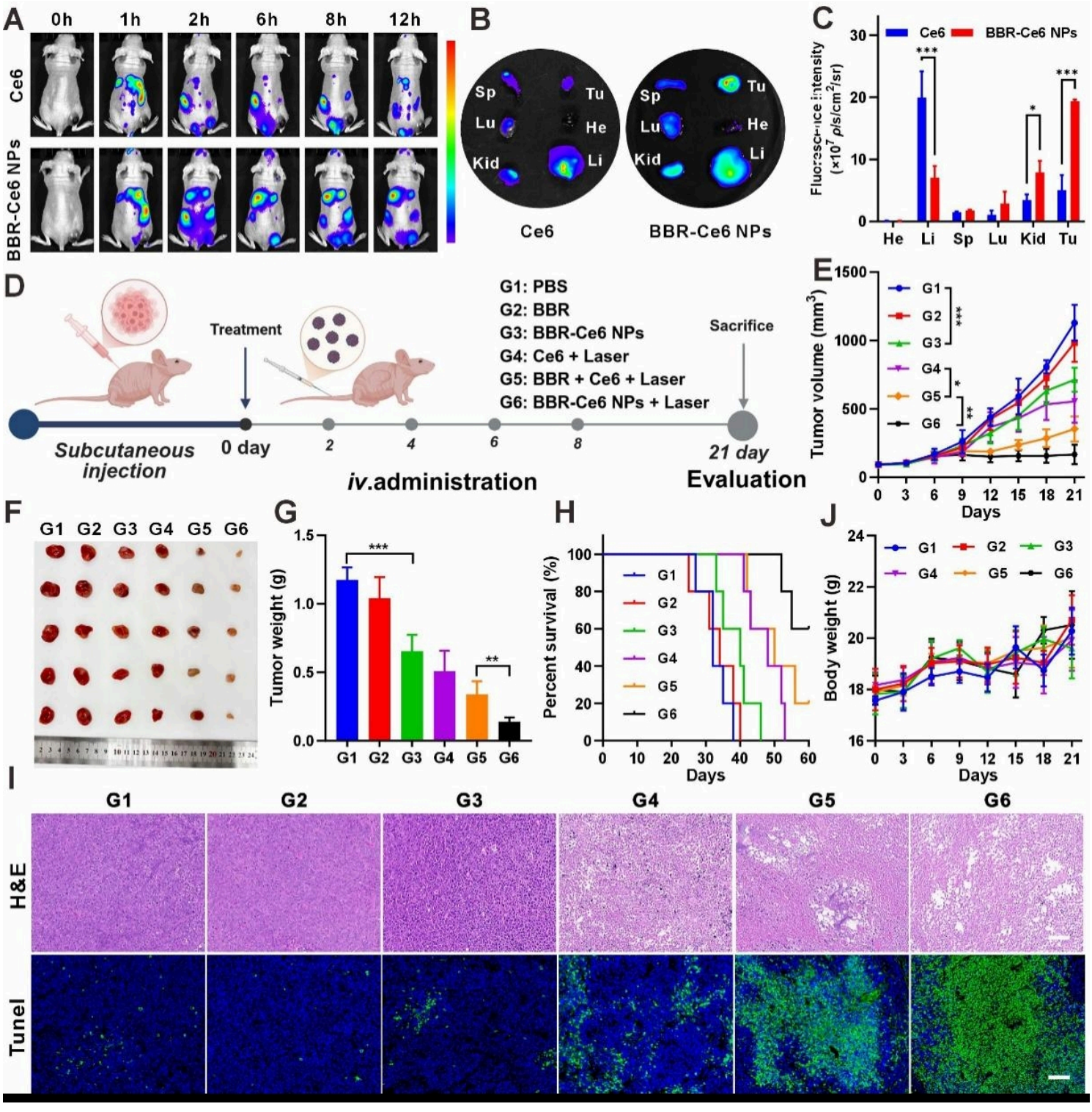


Figure 6

Antitumor studies of BBR-Ce6 NPs *in vivo*. (A) *In vivo* fluorescence images of HepG2 tumor-bearing mice at different time points (0, 1, 2, 6, 8, and 12 h) after intravenous injection of Ce6 or BBR-Ce6 NPs. (B) Ex vivo fluorescence images of organs and tumors after 12 h post administration. (C) Semi-quantitative analysis of the fluorescence intensity of excised tissues and tumors in (B). (D) Diagram of the establishment of tumor-bearing mice and the entire treatment process. (E) Progression of tumor volume in mice under different treatment groups. (F) Photographs of tumor tissues dissected from each treatment group on day 21. (G) The average weight of the tumors dissected from each group after treatment. (H) Body weight changes of HepG2 tumor-bearing mice in G1-G6 groups during the treatment period. (I) Survival curves of mice after different treatments. (J) H&E and TUNEL staining analysis of tumor tissues after various treatments. Scale bar: 100 μm.

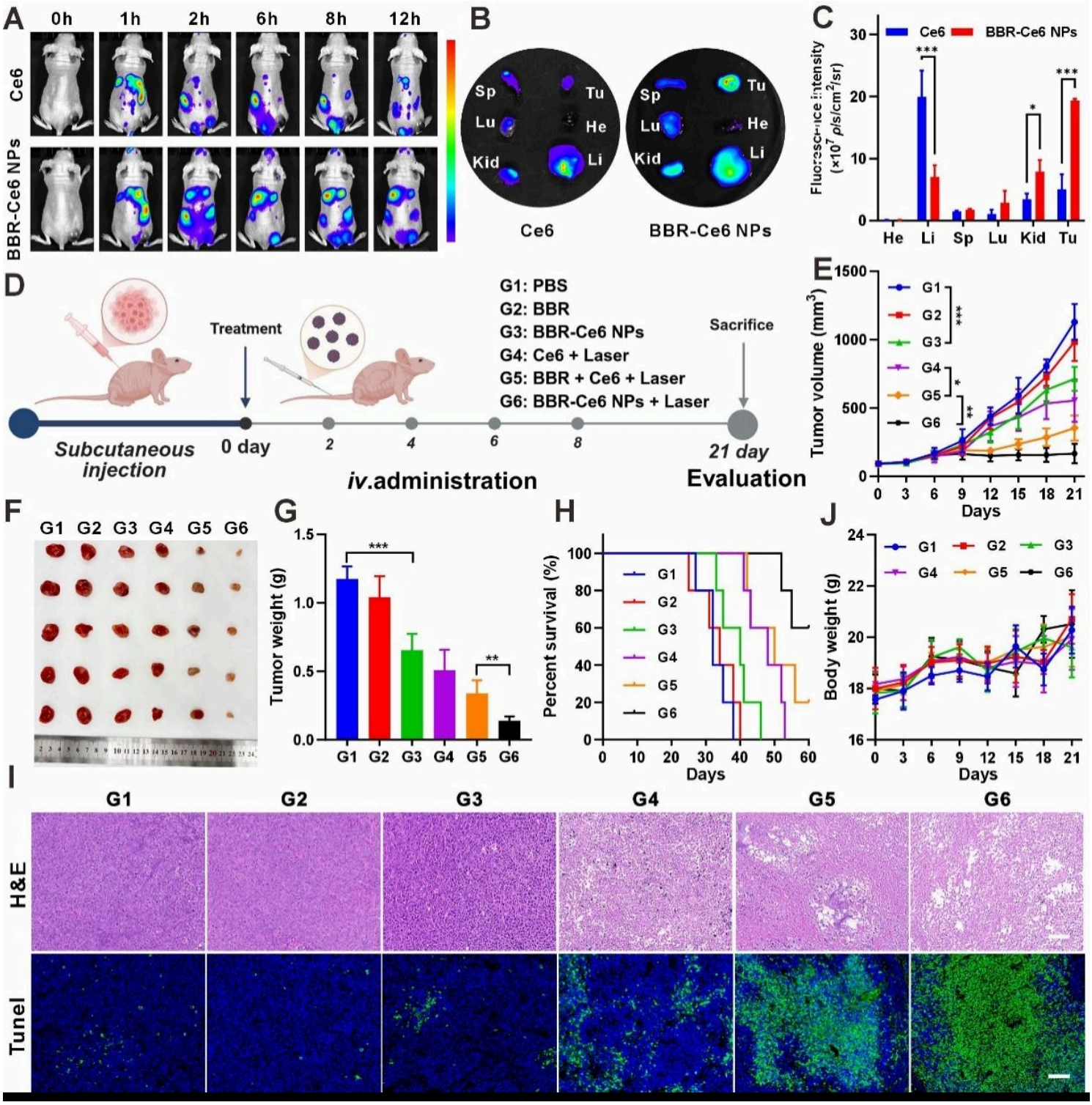


Figure 6

Antitumor studies of BBR-Ce6 NPs *in vivo*. (A) *In vivo* fluorescence images of HepG2 tumor-bearing mice at different time points (0, 1, 2, 6, 8, and 12 h) after intravenous injection of Ce6 or BBR-Ce6 NPs. (B) Ex vivo fluorescence images of organs and tumors after 12 h post administration. (C) Semi-quantitative analysis of the fluorescence intensity of excised tissues and tumors in (B). (D) Diagram of the establishment of tumor-bearing mice and the entire treatment process. (E) Progression of tumor volume in mice under different treatment groups. (F) Photographs of tumor tissues dissected from each

treatment group on day 21. (G) The average weight of the tumors dissected from each group after treatment. (H) Body weight changes of HepG2 tumor-bearing mice in G1-G6 groups during the treatment period. (I) Survival curves of mice after different treatments. (J) H&E and TUNEL staining analysis of tumor tissues after various treatments. Scale bar: 100 μm.

Supplementary Files

This is a list of supplementary files associated with this preprint. Click to download.

- SupportingInformation.docx
- SupportingInformation.docx
- SupportingInformation.docx
- SupportingInformation.docx
- floatimage1.jpeg
- floatimage1.jpeg
- floatimage1.jpeg
- floatimage1.jpeg